

A Novel Pipeline for the Identification of New Gamma-Ray Blazars from the 4FGL-Xiang Catalog Based on Multi-wavelength Flux Distributions

YUNCHUAN XIANG,¹ YINGZHI YE,¹ PENG FENG,¹ XIANKAI PANG,¹ XIAOFEI LAN,¹ AND NINGFENG ZHANG¹

¹*School of Physics and Astronomy, China West Normal University, Nanchong 637009, China*

ABSTRACT

Using 16 years of Fermi-LAT data and resources from the NASA/IPAC Extragalactic Database (NED), we constructed two high-precision catalogs: the updated 4FGL-Xiang-DR2 (DR2) and a supplementary version of the fifth edition of Roma-BZCAT (5BZCAT_err), both featuring refined positional uncertainties. We performed a spatial cross-identification between the two catalogs and developed a systematic three-step analytical pipeline: (1) efficient retrieval of positional uncertainties and multi-wavelength fluxes from 5BZCAT_err, (2) calculation of spatial association probabilities with DR2, and (3) statistical modeling of multi-band fluxes, using the Box-Cox transformation and a truncated normal distribution. Through this process, we identified 17 new blazar candidates. Fermi-LAT analysis reveals that, except for J1043.7+5323, which exhibits significant flux variability above 100 MeV, the remaining sources display stable fluxes, without apparent spatial extension or spectral curvature. Multi-wavelength flux modeling shows that 15 of the 17 sources fall within the 2σ confidence interval of the distribution model, demonstrating strong statistical consistency with known blazar samples. As Fermi-LAT data continues to accumulate, the remaining two sources are expected to converge toward the high-confidence region, providing further support for the common-source hypothesis.

Keywords: Active galactic nuclei (16) — Astrostatistics distributions (1884) — Cross-validation (1909) — Catalogs (205) — Gamma-ray astronomy (628) — Flat-spectrum radio quasars (2163) — BL Lacertae objects (158)

1. INTRODUCTION

Blazars represent the most extreme class of high-energy γ -ray emitters among active galactic nuclei (AGN). Their typical observational properties encompass exceptionally high luminosities, pronounced and rapid variability, intense and highly variable polarization, apparent superluminal motion observed in the radio regime, non-thermal continuum spectra dominated by nuclear emission, and strong γ -ray emission (J. R. P. Angel & H. Stockman 1980; B. J. Wills et al. 1992; A. Abdo et al. 2010a). These observational characteristics primarily arise from Doppler boosting associated with relativistic jets, wherein the jet axis of a blazar aligns closely with our line of sight, significantly amplifying the observed radiation through relativistic beaming (R. Blandford et al. 1978; C. M. Urry & P. Padovani 1995). The intense γ -ray emission exhibited by blazars makes them crucial probes in high-energy astrophysics, particularly for investigating the acceleration mechanisms of cosmic particles and exploring associated astrophysical phenomena (F. Aharonian et al. 2006; F. Tavecchio 2021; I. Liodakis et al. 2022).

Since the launch of the Fermi Large Area Telescope (Fermi-LAT) (W. Atwood et al. 2009), the sample of high-energy blazars has steadily expanded, providing crucial observational constraints for investigating their high-energy emission mechanisms and classification schemes. Based on long-term observational data, the Fermi team has released a series of γ -ray source catalogs (A. A. Abdo et al. 2010; P. L. Nolan et al. 2012; F. Acero et al. 2015; S. Abdollahi et al. 2022; J. Ballet et al. 2023). The latest γ -ray catalog of AGN released by the Fermi collaboration, 4LAC-DR3², includes 3,407 high-latitude and 407 low-latitude high-energy AGNs, the vast majority of which are blazars (M. Ajello et al. 2022a). These long-term observational results have significantly advanced our understanding of the

Email: xiang_yunchuan@yeah.net

² <https://fermi.gsfc.nasa.gov/ssc/data/access/lat/4LACDR3/>

statistical properties of blazars in the γ -ray band and provided a valuable dataset for investigating their classification and evolutionary differences.

Blazars are primarily classified into two categories: flat-spectrum radio quasars (FSRQs) and BL Lacertae objects (BL Lacs). FSRQs exhibit prominent broad emission lines with an equivalent width ($\text{EW} > 5 \text{ \AA}$) (C. M. Urry & P. Padovani 1995). Their spectra reveal a significant contribution from accretion disk radiation, and they typically have a relatively high Eddington ratio $L_{\text{BLR}}/L_{\text{Edd}} \sim 5 \times 10^{-4}$ (G. Ghisellini et al. 2011). In contrast, BL Lacs display weaker spectral features, often lacking prominent emission lines ($\text{EW} < 5 \text{ \AA}$) (C. M. Urry & P. Padovani 1995), with jet emission dominating their radiation and minimal contribution from the accretion disk (T. Sbarrato et al. 2012). Based on the synchrotron peak frequency ($\nu_{\text{peak}}^{\text{S}}$), blazars can be further classified into three subtypes: low-synchrotron-peaked (LSP, $\log \nu_p < 14 \text{ Hz}$), intermediate-synchrotron-peaked (ISP, $14 \leq \log \nu_p \leq 15 \text{ Hz}$), and high-synchrotron-peaked (HSP, $\log \nu_p > 15 \text{ Hz}$) (A. Abdo et al. 2010a).

The non-thermal radiation characteristics of blazars originate from particle acceleration mechanisms within their jets. The prevailing acceleration mechanisms include Fermi acceleration and magnetic reconnection. In the upstream and downstream regions of shocks within the jet, charged particles can undergo repeated scattering through first-order Fermi acceleration, gaining energy and forming a power-law energy spectrum of high-energy electrons or protons (R. Blandford & D. Eichler 1987). By contrast, second-order Fermi acceleration occurs in a turbulent magnetic field environment, where particles gradually accumulate energy through stochastic scattering (L. Stawarz & V. Petrosian 2008). Additionally, magnetic reconnection regions within the jet can locally release magnetic energy and rapidly accelerate particles to high energies. This mechanism effectively explains the rapid γ -ray flares observed in some blazars on minute timescales (D. Giannios et al. 2009; L. Sironi & A. Spitkovsky 2014).

The high-energy radiation mechanisms of blazars are primarily explained by leptonic and hadronic models. The leptonic model includes two main processes: synchrotron self-Compton scattering (SSC) and external Compton scattering (EC), whereas the hadronic model involves proton-proton (pp) or proton-photon ($p\gamma$) interactions. In FSRQs, due to the presence of intense accretion disk radiation and broad-line region (BLR) photon fields, high-energy emission is typically dominated by the EC process. In this scenario, relativistic electrons in the jet scatter photons originating from the accretion disk, BLR, or dust torus up to the GeV energy range (M. Sikora et al. 1994; G. Ghisellini et al. 1998; M. Ackermann et al. 2015). In comparison, BL Lacs—particularly the high-synchrotron-peaked (HSP) subclass—lack significant external photon fields, and their high-energy γ -ray emission is primarily produced through the SSC process. In this mechanism, relativistic electrons in the jet scatter their own synchrotron photons to TeV energies (L. Maraschi et al. 1992; F. Tavecchio et al. 2001; A. Abdo et al. 2010b). In hadronic models, protons are accelerated to ultrarelativistic energies, and the high-energy emission is dominated by proton-synchrotron emission and photons from π^0 decay (K. Mannheim & P. Biermann 1992; K. Mannheim 1993; F. Aharonian 2000; A. Mücke & R. Protheroe 2001; A. Mücke et al. 2003).

The Roma-BZCAT is one of the most comprehensive blazar catalogs, initially compiled and continuously updated by E. Massaro et al. (2009). This catalog identifies blazars through optical spectroscopy and integrates multi-wavelength observational data. The latest version, the fifth edition (5BZCAT)³ published in 2015, includes 3,561 blazars, comprising 1,151 BL Lacs (5BZB), 1,909 FSRQs (5BZQ), and 227 uncertain blazar candidates (5BZU). Additionally, a new category, denoted as 5BZG, was introduced in the 5BZCAT catalog. This category encompasses sources that are typically reported as BL Lac objects in the literature but exhibit a spectral energy distribution (SED) characterized by significant dominance of the galaxian emission over the nuclear one. The 5BZG category contains a total of 274 sources (E. Massaro et al. 2015). With its rigorous classification criteria and extensive multi-wavelength data, 5BZCAT has become an essential database for investigating the statistical and physical properties of blazars.

Y. Xiang et al. (2024) successfully developed an all-sky automated algorithm for identifying new γ -ray sources based on the advanced numerical algorithms of **Fermipy** (M. Wood 2017) and the Galactic diffuse background model. This algorithm divides the entire sky into 72 regions and employs multi-threaded parallel computing, significantly enhancing the efficiency of new source searches. Y. Xiang et al. (2024) applied this algorithm for the first time to analyze 15.41 years of all-sky survey data from Fermi-LAT, ultimately identifying 1,379 new γ -ray sources with a significance above 4σ , among which 497 sources exceeded 5σ significance. This achievement substantially expands the number of γ -ray sources, and these newly detected sources have been compiled into a unified catalog named “4FGL-Xiang”.

³ <https://www.ssdsc.asi.it/bzcat/>

At the outset, we conducted a systematic survey of source classifications in 4FGL-DR4⁴, and found that AGNs⁵ account for 56.3% of the total γ -ray sources in the entire catalog. Among these AGNs, blazars constitute 57%, indicating that blazars are among the most prevalent γ -ray sources in the all-sky survey. Given the substantial proportion of blazars and the fact that the γ -ray sources in 4FGL-Xiang catalog (DR1) have not yet been cross-identified with other catalogs, we are strongly motivated to investigate the potential associations between the newly detected γ -ray sources in DR1 and blazars listed in 5BZCAT. Identifying and confirming more blazar candidates, along with analyzing the statistical properties of BZBs and BZQs based on existing blazar samples, is of great significance for studying the classification, evolution, jet dynamics, non-thermal radiation mechanisms, and contributions of blazars to the cosmic high-energy background (A. Abdo et al. 2010b; M. Volonteri et al. 2011; F. Massaro et al. 2012; M. Ackermann et al. 2015; M. Ajello et al. 2015; M. G. Baring et al. 2017). In Section 2, we provide a detailed description of our data analysis methods and results, while Section 3 presents a discussion and summary of our findings.

2. DATA ANALYSIS

2.1. Construction of the 4FGL-Xiang-DR2 Including Elliptical Positional Uncertainties

Prior to conducting data analysis, we reviewed the limitations and improvements of DR1, which primarily include the limited degrees of freedom in defining the region of interest (ROI) and the absence of elliptical positional uncertainty. These issues are discussed in detail below, along with the corresponding improvement measures.

The limited degrees of freedom in the ROI pose challenges for analysis in DR1 (Y. Xiang et al. 2024). Accurate background fitting is critical in Fermi-LAT data analysis. In a binned likelihood analysis, Y. Xiang et al. (2024) set the ROI as a circular area with a 5-degree radius centered on the target position, and freed the spectral parameters of all sources within this area to investigate residual background radiation within a larger $30^\circ \times 30^\circ$ square region. By analyzing the position and significance level of the surrounding residual emission, Y. Xiang et al. (2024) identified 1,379 new γ -ray sources. For sources detected beyond the 5-degree radius, the limited degrees of freedom in the spectral parameters of surrounding background sources, combined with the broad point-spread function (PSF) of low-energy band, increased the probability of contamination from background noise during fitting, potentially reducing the accuracy of the significance levels of these new sources. To address this, we referred to a precise background radiation simulation scheme, centered on the target source, as recommended by the Fermi Science Support Center⁶, to re-evaluate the significance levels and related parameters of the 1,379 new γ -ray sources. DR1 lacks key elliptical positional uncertainty information. The localization accuracy of a source is primarily determined by the spatial distribution of a limited number of high-energy photons. Due to statistical fluctuations in the arrival directions of these photons, the resulting positional uncertainty often deviates from an ideal circular shape. In the early stages of Fermi data analysis, the circular positional uncertainty was adopted as a rough approximation and applied in the Fermi-LAT Bright Source List (BSL; A. A. Abdo et al. 2009). This is because the bright γ -ray sources included in the BSL typically have high Test Statistic (TS) values and a sufficient number of high-energy photons, which make the asymmetry in the positional uncertainty distribution relatively minor. As a result, the circular approximation has only a limited impact on the analysis outcomes in such cases.

Based on observational data, the Fermi team constructed a likelihood function to characterize the probability distribution of point source positions. This function can be used to estimate the positional uncertainty of a source, and its width is proportional to the width of the PSF. The positional uncertainty of a source is typically represented by an elliptical distribution that defines the region of uncertainty on the sky. An error ellipse is uniquely defined by five parameters: the right ascension and declination of its center, the lengths of the semi-major and semi-minor axes, and the orientation angle of the ellipse (A. A. Abdo et al. 2010). At the 95% confidence level, there is an approximate relationship between the semi-major and semi-minor axes of the elliptical positional uncertainty (denoted as $\sigma_{x,95}$ and $\sigma_{y,95}$, respectively) and the corresponding circular positional uncertainty (r_{95}) (A. Abdo et al. 2010a): $r_{95} = \sqrt{\sigma_{x,95} \times \sigma_{y,95}}$. Compared to circular positional uncertainty, which has three degrees of freedom, elliptical positional uncertainty involves five degrees of freedom and can therefore more accurately represent the true distribution of observational errors at the same confidence level. Since the release of the 1FGL, elliptical positional uncertainty has

⁴ https://fermi.gsfc.nasa.gov/ssc/data/access/lat/14yr_catalog/

⁵ The AGN subclasses include agn, bcu, bll, css, fsrq, nlsy1, rdg, sey, and ssrq, with detailed explanations available at <https://heasarc.gsfc.nasa.gov/W3Browse/fermi/fermilpsc.html>.

⁶ <https://fermi.gsfc.nasa.gov/ssc/data/access/lat/BackgroundModels.html>

been recognized as an important parameter and consistently included in subsequent Fermi-LAT source catalogs (e.g., A. A. Abdo et al. 2010; P. L. Nolan et al. 2012; F. Acero et al. 2015; S. Abdollahi et al. 2020).

As shown in Figures 2 and 3 of A. A. Abdo et al. (2010), γ -ray sources with higher TS values and harder spectra tend to have smaller 95% confidence-level positional uncertainties. This is primarily due to the narrower PSF at higher energies. This trend indicates that bright γ -ray sources with harder spectra and a greater number of high-energy photons generally achieve better localization accuracy compared to sources with softer spectra and fewer high-energy photons. We subsequently investigated the distributions of TS values, spectral indices, and r_{95} for sources in the DR1, as illustrated in Figure 1. The left panel shows that the average spectral index is 2.25, with more than 46% of the sources

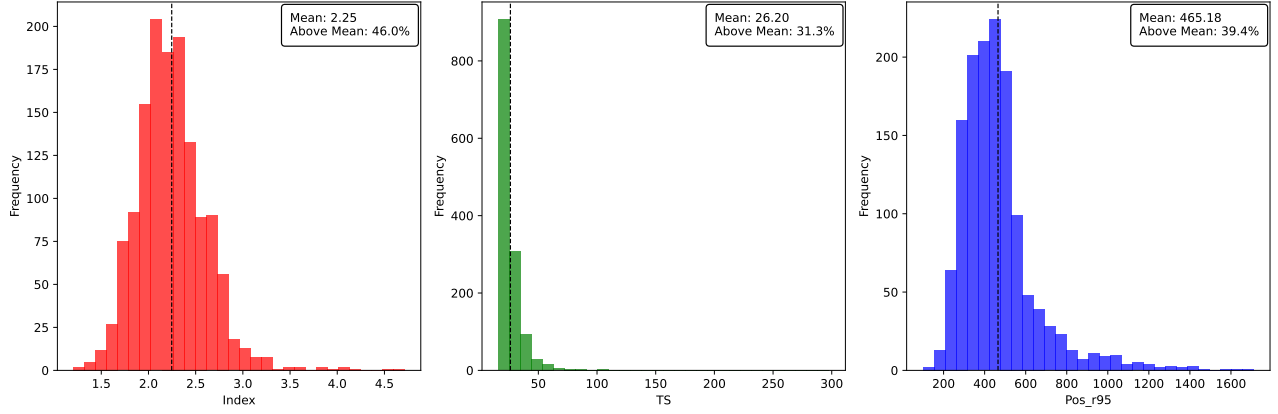


Figure 1. Distributions of spectral index (left), TS values (middle), and r_{95} positional uncertainties (right) for sources in the DR1. In all panels, the vertical black dashed line marks the mean value.

exhibiting values above this average, indicating that the majority of sources have relatively soft spectra. The middle panel reveals a mean TS value of 26.3, with approximately 68.7% of the sources falling below this level, suggesting that most DR1 sources are weak γ -ray emitters. The right panel shows that the average r_{95} positional uncertainty is 465.18". In Section 2.3, we obtained the average length of the semi-major axis of the 95% confidence-level elliptical positional uncertainties for the 5BZCAT_err sample, which is approximately 4". In comparison, the positional uncertainties in DR1 are nearly two orders of magnitude larger than those in 5BZCAT_err, further emphasizing the lower localization accuracy of Fermi-LAT sources.

The above analysis indicates that most sources in DR1 are faint γ -ray sources, generally exhibiting relatively soft spectral characteristics. In addition, their elliptical positional uncertainties are significantly larger than those of the sources in the 5BZCAT_err. Given the directional asymmetry of positional uncertainties, approximating them using circular error models may increase the risk of mismatches in spatial cross-identification. The use of a high-precision elliptical positional uncertainty model is essential for improving the accuracy and reliability of subsequent spatial cross-identification.

To address the aforementioned limitations, in this analysis, we employed the Fermi-LAT data analysis toolkit **Fermipy** (version 1.2.0) to investigate γ -ray sources at specified positions. Referring to the standard Binned Likelihood Tutorial provided by the Fermi Science Support Center ⁷, we performed a binned likelihood analysis for each γ -ray source in DR1, centered on its coordinates. The analysis utilized the Pass 8 photon dataset (P8R3_V3), with the instrument response function (IRF) set to P8R3_SOURCE_V3. Photon events were filtered using the criteria **evtype** = 3 and **evclass** = 128. The energy binning was configured with 10 bins per decade (**binsperdec** = 10), and the spatial resolution was set to 0°.1 (**binsz** = 0°.1), and the photon energy range spanned 100 MeV to 1 TeV. The selected time range extended from August 4, 2008 (MET 239557417) to August 29, 2024 (MET 745981270). To minimize contamination from Earth-limb atmospheric cosmic rays, the maximum zenith angle was restricted to 90° (**zmax** = 90°). The input model files for the likelihood analysis included all sources within a 15° radius of the center of each analysis region from both the 4FGL-DR4 and DR1. For sources within a 6° radius of each ROI, the normalization factor and spectral index were set as free parameters during the likelihood fitting. Additionally, the normalization parameters for

⁷ https://fermi.gsfc.nasa.gov/ssc/data/analysis/scitools/binned_likelihood_tutorial.html

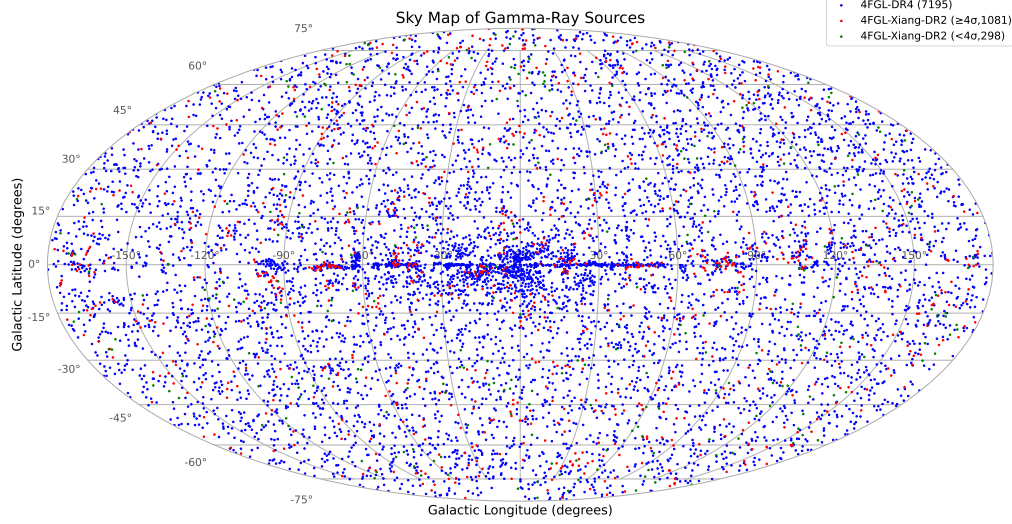


Figure 2. Sky map showing the spatial distribution of γ -ray sources from 4FGL-DR4 (blue, 7,195 sources) and sources in DR2 with significance $\geq 4\sigma$ (red, 1,081 sources) and $< 4\sigma$ (green, 298 sources).

the two diffuse background templates, namely the Galactic diffuse emission (`gll_iem.v07.fits`) and the extragalactic isotropic diffuse emission (`iso_P8R3_SOURCE_V3.v1.txt`)⁸, were also allowed to vary freely in the likelihood fitting.

We first employed the **GTAnalysis** module to load the configuration file containing the aforementioned parameters, to perform the initial setup and optimization procedures. Prior to conducting the binned likelihood fit, we invoked the `optimize()` function, which employs an iterative strategy to automatically optimize the fit for all sources within the ROI. Running this method early in the analysis typically ensures that all parameters are close to the global likelihood maximum, thereby improving the efficiency of subsequent fits and accelerating convergence. Next, we performed the likelihood fit using the `fit()` function, specifying **NEWMINUIT** as the likelihood optimizer (`optimizer='NEWMINUIT'`) and setting `min_fit_quality=3` to ensure that the fit results for each source reached an optimal state.

We then used the `gta.localize()` function to refine the position of each target source by determining its best-fit coordinates and associated elliptical positional uncertainty. By enabling the `update=True` option, the optimized coordinates were automatically substituted for the original ones, thereby ensuring positional accuracy. After obtaining the best-fit positions, we re-ran the `fit()` function to confirm that all relevant parameters were optimized at the updated locations. Based on the above procedure, we compiled the fit results for 1,379 γ -ray sources and incorporated them into a new catalog, 4FGL-Xiang-DR2 (DR2). The complete catalog was saved in FITS format and deposited in the China-VO Paper Data Repository (see Section 5).

The parameter information for DR2 is presented in Table 6. Compared to DR1, this version provides more comprehensive and detailed source parameters, including elliptical positional uncertainties, photon fluxes, and energy fluxes across different energy bands, which were not included in DR1. Subsequently, we compared the significance levels of the 1,379 sources between DR2 and DR1. The results show that 298 faint GeV sources, which had an average significance level of 4.5σ in DR1, exhibit reduced significance levels in DR2, falling below the 4σ threshold.

2.2. Exploring the Decline in Detection Significance of 298 DR1 Sources

To investigate the causes of the TS value decline for the 298 sources, we examined their significance levels above 500 MeV ($\text{Sig}_{0.5}$) in DR1. The results show that their $\text{Sig}_{0.5}$ values range from 4.01 to 5.91σ , with 93.29% of the sources falling below the 5σ threshold. This suggests that the majority of these objects are intrinsically weak γ -ray emitters. Moreover, the average photon count above 500 MeV (N_p) for these sources was only 115, significantly lower

⁸ <https://fermi.gsfc.nasa.gov/ssc/data/access/lat/BackgroundModels.html>

than the DR1 sample average of 238. These results indicate that these faint sources originally contained relatively few high-energy photons, making their TS values—already near the 4σ detection threshold—susceptible to fluctuations due to variations in spectral parameters and background noise (Y. Xiang et al. 2024).

In this analysis, we referred to the target-centered strategy recommended by the Fermi Science Support Center and expanded the ROI radius from 5° to 6° , allowing more surrounding sources and diffuse components to be included and modeled with increased degrees of freedom. This strategy, combined with refined background, spectral, and spatial models in DR2, may have contributed to a more realistic representation of the γ -ray environment. In the likelihood analysis process, some photons previously attributed to the target sources might have been reassigned to nearby sources or background, potentially leading to a reduction in TS values for 298 faint GeV sources.

In *Fermi*-LAT data analysis, it is common for the significance levels of certain sources to decrease with the accumulation of data and the updating of catalog parameters. This phenomenon is substantiated by a comparative analysis of the average significance level (**Signif_Avg**) values for 6,599 sources across the 4FGL-DR3 (`gll_psc_v31.fit`) and 4FGL-DR4 (`gll_psc_v35.fit`) catalogs. As shown in Table 1, 1,931 sources in 4FGL-DR4 exhibit the lower **Signif_Avg** values compared to their corresponding values in 4FGL-DR3, with a **Ratio_Sig** (defined as the ratio of **Signif_Avg_v35** to **Signif_Avg_v31**) less than 1. This finding suggests that, with the accumulation of observational data and updates to the spectral and spatial model parameters, approximately 30% of the sources exhibit a decline in significance level. This finding strongly supports the conclusion that decreases in significance levels are a common

Table 1. Comparison of **Signif_Avg** and **Energy_Flux100** between 4FGL-DR3 and 4FGL-DR4

Source_Name	RAJ2000	DEJ2000	Signif_Avg_v31	Energy_Flux100_v31	Signif_Avg_v35	Energy_Flux100_v35	Ratio_Sig	Ratio_Eflux
4FGL J0000.3-7355	0.098	-73.922	7.460	1.58E-12	8.493	1.74E-12	1.138	1.097
4FGL J0000.5+0743	0.138	7.727	5.272	1.12E-12	5.681	1.93E-12	1.078	1.721
4FGL J0000.7+2530	0.188	25.515	4.177	8.57E-13	4.197	8.05E-13	1.005	0.939
...

Note. Please refer to Table 6 for definitions and units of the keywords. The complete dataset can be found in the file `Comparison_v31_v35.xlsx`, as referenced in Section 5.

phenomenon in *Fermi*-LAT data analysis. However, unlike 4FGL-DR4, which retained 322 sources with **Signif_Avg** values below 4σ , we excluded such low-significance sources to enhance the statistical reliability of the sample and minimize background confusion in subsequent spectral and temporal variability analyses. As a result, 1,082 sources were ultimately included in DR2. Additionally, we plotted the spatial distribution of sources from DR2 and 4FGL-DR4 in Figure 2. The results suggest that, except for a relatively higher density of sources along the Galactic plane, DR2 sources are approximately uniformly distributed across the entire sky.

2.3. Construction of the Roma-BZCAT Including Elliptical Positional Uncertainties

Currently, 5BZCAT contains 3,561 sources across four types—5BZQ, 5BZB, 5BZU, and 5BZG—and provides preliminary classifications along with multi-wavelength flux data (E. Massaro et al. 2015). However, 5BZCAT does not include positional uncertainty information, which presents significant challenges for probabilistic spatial cross-matching analyses. The NED⁹ is an online astronomical database maintained by NASA in collaboration with the Infrared Processing and Analysis Center (IPAC) at the California Institute of Technology. It specializes in compiling comprehensive information on extragalactic objects and is continuously updated with the latest astronomical observations and research findings to ensure the timeliness and reliability of its data.

To obtain a catalog of blazar candidates with complete positional uncertainty information, we integrated the data from the 5BZCAT and the NED. First, we automatically obtained the positional uncertainties for the vast majority of sources, and for the few sources that were missing positional errors, we used a positional cross-identification method to complete their missing positional information. Finally, we constructed a new catalog named 5BZCAT_err, which contains the complete positional information for 3,561 sources, for subsequent cross-matching analysis. The detailed construction process for this catalog is described in Appendix A. In the cross-matching analysis described in Section 2.4, 5BZCAT_err served as the blazar candidate catalog for DR2 in subsequent analysis.

⁹ <https://ned.ipac.caltech.edu/>

Table 2. Cross-Matching Results Between DR2 and 5BZCAT_err

DR2_name	DR2_RA	DR2_DEC	5BZ_name	5BZ_RA	5BZ_DEC	Sep	Psingle	Pany	Pi
J1216.2+3451	183.999	34.800	5BZQ J1215+3448	183.982	34.804	53.762	0.99585325	0.9958525	0.9999768
J1219.9+0200	185.069	2.029	5BZQ J1220+0203	185.050	2.062	136.678	0.9969872	0.99698657	1
J1342.3-2901	205.637	-28.970	5BZQ J1342-2900	205.564	-29.012	274.991	0.9892003	0.9891981	1
J1012.0+2313	153.074	23.243	5BZQ J1012+2312	153.068	23.204	141.115	0.99717826	0.99717766	1
J0756.6-1534	119.212	-15.682	5BZQ J0756-1542	119.211	-15.702	70.995	0.99867225	0.998672	1
J1411.6+3407	212.910	34.070	5BZB J1411+3404	212.919	34.073	29.595	0.99883926	0.998839	1
J1221.3+0825	185.377	8.384	5BZG J1221+0821	185.384	8.362	80.453	0.9964194	0.99641865	1
J1004.4+3750	151.173	37.857	5BZB J1004+3752	151.187	37.870	58.542	0.9991889	0.9991887	1
J1207.0-1746	181.811	-17.766	5BZB J1207-1746	181.798	-17.768	44.797	0.99982196	0.9998219	1
J0643.4+4215	100.882	42.210	5BZG J0643+4214	100.862	42.239	117.116	0.99850804	0.99850774	1
J0742.9+3021	115.652	30.390	5BZB J0742+3018	115.679	30.310	299.750	0.994547	0.9945459	1
J0250.4-2130	42.546	-21.479	5BZB J0250-2129	42.579	-21.495	122.862	0.99928904	0.9992889	1
J1243.9+4046	191.004	40.730	5BZQ J1243+4043	190.982	40.733	59.848	0.99754095	0.9975405	1
J1336.8+0040	204.300	0.440	5BZB J1337+0035	204.381	0.591	617.766	0.8839802	0.8839588	1
J1043.7+5323	161.024	53.376	5BZQ J1044+5322	161.044	53.372	46.200	0.9996606	0.9996605	1
J1531.7+0845	232.879	8.867	5BZG J1531+0852	232.899	8.864	71.387	0.99670756	0.9967069	1
J0205.4+1441	31.298	14.740	5BZQ J0205+1444	31.305	14.742	23.726	0.9988691	0.9988689	1

Note. Please refer to Table 6 for keyword explanations and units.

2.4. Cross-Matching Analysis Between DR2 and 5BZCAT_err

nway is a numerical analysis software based on Bayesian statistics, specifically designed for multi-wavelength source cross-matching. It effectively incorporates positional uncertainties, magnitude information (or other priors) to compute matching probabilities, thereby improving the accuracy of cross-identification. In multi-wavelength cross-matching analysis, magnitude serves as an important prior in the computation of matching probabilities. Incorporating magnitude information can effectively reduce mismatches that may arise from relying solely on positional data, which is particularly important in cases of high source density or relatively large observational uncertainties (M. Salvato et al. 2018). M. Ackermann et al. (2015) examined the distribution characteristics of blazars in the Roma-BZCAT, comparing those detected and undetected by Fermi-LAT across three wavebands: radio flux density at 1.4 GHz, optical R-band magnitude, and X-ray flux in the 0.1–2.4 keV waveband. The results indicate that γ -ray-bright blazars are, on average, brighter in all three bands, consistent with earlier studies (M. Ackermann et al. 2011; M. Lister et al. 2011). This observed correlation supports the use of magnitude as a prior in cross-matching analyses.

We performed a probabilistic cross-matching between DR2 and 5BZCAT_err using **nway**. To improve accuracy, we adopted an elliptical error model and incorporated optical magnitude information as a prior distribution. We identified high-confidence candidates by applying stringent probabilistic thresholds, requiring the match probabilities (p_{any} and p_i) to each exceed 85%. This process yielded 17 matched pairs. These results were consistently verified using the cross-matching tool in **TOPCAT** and independently validated through visual inspection of their spatial correlations in **DS9**, confirming a high degree of association for the matched pairs. A detailed description of the methodology and verification process can be found in Appendix B.

2.5. Analysis 17 New Candidate Blazar GeV Emission Characteristic

In Section 2.4, we identified 17 newly discovered GeV blazars. Investigating the high-energy emission properties of blazars—including their spatial distribution, spectral characteristics, and variability behavior—holds substantial scientific value for advancing our understanding of their physical mechanisms, radiation processes, and potential contributions to the cosmic-ray background (G. a. Fossati et al. 1998; M. Ajello et al. 2015; C. D. Dermer & B. Giebels

2016; G. Madejski & M. Sikora 2016). In this section, we systematically analyze the fundamental emission properties of these 17 sources using the **Fermipy** package.

2.5.1. γ -Ray Spatial Distribution Analysis

In this study, we conducted a spatial extension analysis of the 17 previously identified sources using the **extension()** function to evaluate their spatial distribution characteristics. For each source, we calculated the spatial extension significance (TS_{ext}) and adopted the criterion proposed by J. Lande et al. (2012), which defines a source as significantly extended if $\text{TS}_{\text{ext}} > 16$. The extension significance is defined as: $\text{TS}_{\text{ext}} = 2 \log \left(\frac{L_{\text{ext}}}{L_{\text{ps}}} \right)$, where L_{ext} and L_{ps} denote the likelihood values for the extended and point source models, respectively.

In our analysis, we applied two spatial extension templates—the two-dimensional Gaussian (2D-Gaussian) and the uniform disk (Disk) models—for source fitting. The radius (σ) of the spatial models was set to range from 0.1° to 3.0° with a step size of 0.01° . The threshold for spatial extension significance was set to $\text{TS}_{\text{ext}} = 16$ (corresponding to **Tsqrts_threshold = 4.0**), and the **update** parameter was set to **True** to ensure that the best-fit spatial model adopted for subsequent analyses. By comparing the fitting results from the two spatial models, we found that the TS_{ext} values derived from both the 2D-Gaussian ($\text{TS}_{\text{ext, Gauss}}$) and Disk ($\text{TS}_{\text{ext, Disk}}$) models were below the threshold of 16 for all 17 sources (see Table 3), indicating that none of the sources exhibit significant spatial extension. Consequently, the point source model was adopted as the best-fit model for all 17 sources in subsequent analyses.

2.5.2. Spectral Analysis

To investigate the spectral curvature properties of the sources, we calculated the widely used spectral curvature index, TS_{cur} , defined as $\text{TS}_{\text{cur}} = 2(\log L_{\text{curved spectrum}} - \log L_{\text{power law}})$. According to P. L. Nolan et al. (2012), a source is considered to exhibit significant spectral curvature if $\text{TS}_{\text{cur}} > 16$. In this study, we employed the **curvature()** function from **Fermipy** to compute the TS_{cur} values for each target source under two commonly used spectral models: the Log-Parabola (LP) model and the Power-Law with Super-Exponential Cutoff (PLEC) model.

We performed spectral fitting above 100 MeV using both spectral models and calculated the corresponding TS_{cur} values to evaluate whether they exceeded the threshold of 16. The results show that, for all 17 sources, both $\text{TS}_{\text{cur, LP}}$ and $\text{TS}_{\text{cur, PLEC}}$ values are below 16 (see Table 3), indicating that none of the sources exhibit significant spectral curvature. Consequently, the power-law (PL) model was adopted as the best-fit spectral model for all subsequent analyses. The SEDs of three representative GeV blazars—(a) J1043.7+5323, (b) J1016.3+4104, and (c) J1256.6+0606—are shown in Figure 3. All spectral data are compiled into the **SED17.tar.xz** archive, which is available in Section 5.

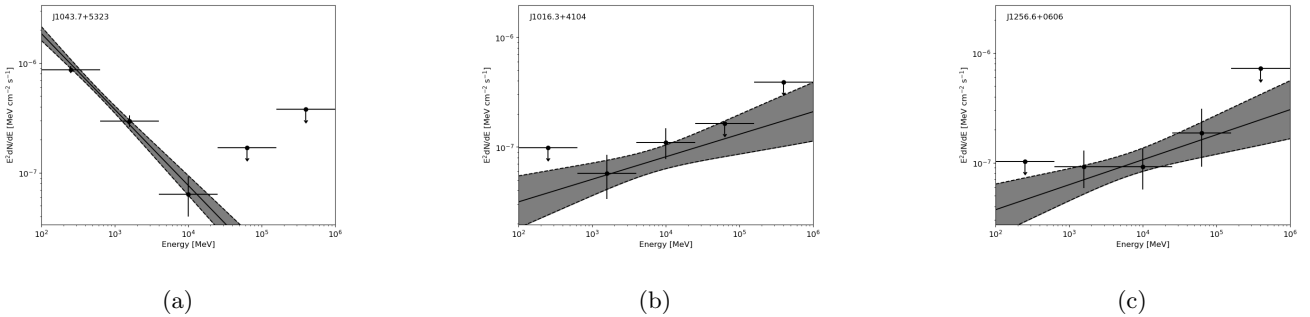


Figure 3. SEDs of three representative GeV sources: (a) J1043.7+5323, (b) J1016.3+4104, and (c) J1256.6+0606. The black data points represent the binned photon flux measurements with 1σ error bars, where data points with TS values less than 4 are replaced by the 95% confidence level upper limits. The black lines indicate the best-fit PL models, and the shaded regions represent the 1σ uncertainties of the fits.

2.5.3. Variability Analysis

In this study, we performed variability analyses for 17 sources using the **lightcurve()** function. Each source’s light curve (LC) was divided into 16 time bins, with each bin corresponding to one year. Following the method proposed by P. L. Nolan et al. (2012), we calculated the variability index TS_{var} for each source (see Table 3). According to

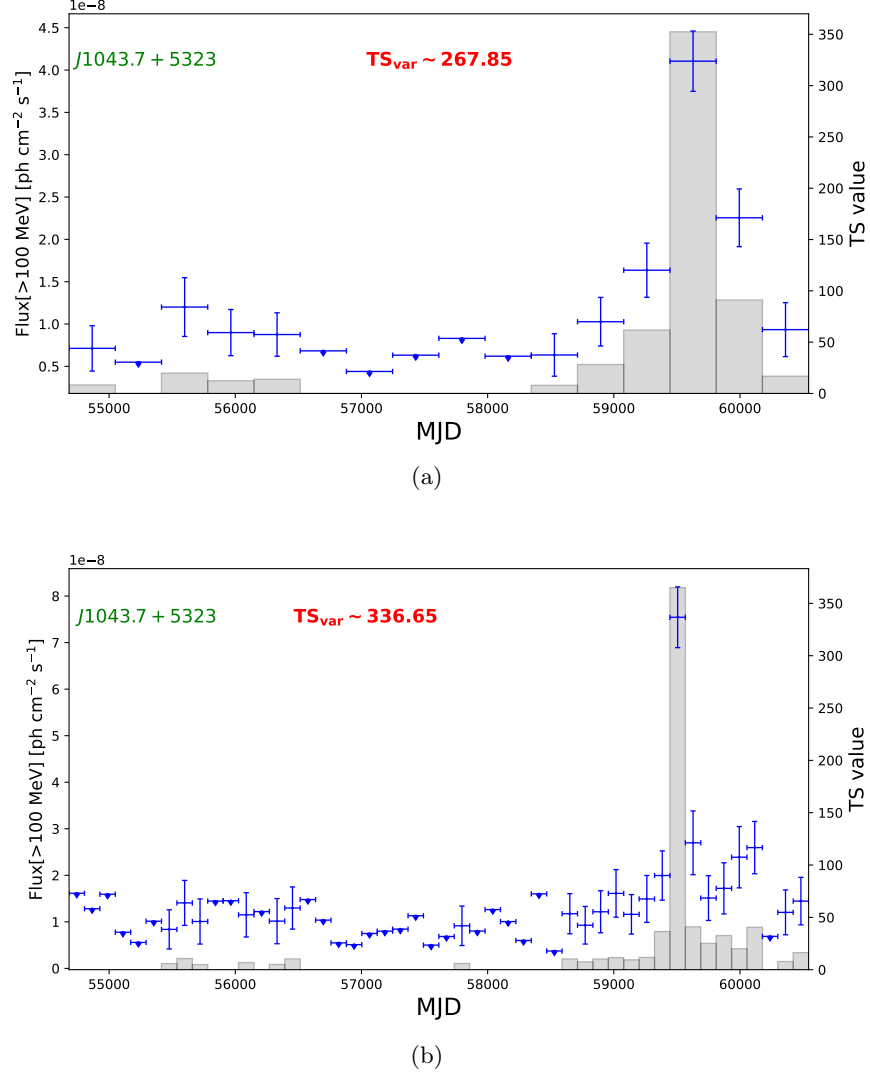


Figure 4. LCs of J1043.7+5323 above 100 MeV using different time binnings. The x-axis represents the Modified Julian Date (MJD) in days. (a) LC with yearly binning (16 time bins) yields a variability index of $TS_{\text{var}} \approx 267.85$; (b) LC with 4-month binning (48 time bins) shows a variability index of $TS_{\text{var}} \approx 336.65$. Blue points represent the photon fluxes with 1σ uncertainties, where data points with TS values < 4 are replaced by 95% confidence level upper limits. Gray bars indicate the TS values for each time bin.

statistical criteria, a source is considered significantly variable at the 99% confidence level if $TS_{\text{var}} > 30.58$, in which case the source can be identified as variable. Our analysis revealed that among the 17 sources, J1043.7+5323 exhibited a high variability index of $TS_{\text{var}} = 267.85$, above the threshold, indicating significant flux variations in its LC, see Figure 8(a). To further investigate this behavior, we generated a LC for J1043.7+5323 with a finer time binning of four months per bin. The result still showed significant variability, with $TS_{\text{var}} = 336.65$, exceeding the corresponding 99% confidence threshold of 72.44, see Figure 8(b). For the remaining 16 sources, no significant variability was observed in their LCs. All LCs are compiled in the file `LC17.tar.xz`, accessible via Section 5.

2.6. Statistical Analysis of Multi-Wavelength Flux Distributions of 17 New GeV Blazar Candidates

Blazars are a special class of AGN whose powerful relativistic jets produce broadband emission spanning the electromagnetic spectrum, from radio to high-energy gamma rays. This makes them ideal natural laboratories for studying extreme physical processes in the Universe, such as jet formation and acceleration, and high-energy emission mechanisms. Based on their optical spectra, blazars are typically classified into two subclasses, BZB and BZQ, a division

Table 3. Fitting Results of Spatial Models for 17 Sources

Name_5BZCAT	Name_DR2	TS _{cur,lp}	TS _{cur,plec}	TS _{ext,disk}	TS _{ext,gauss}	TS _{var}
5BZB J1411+3404	J1411.6+3407	0.00	0.63	1.02	0.17	8.65
5BZG J1221+0821	J1221.3+0825	5.06	5.07	3.17	2.62	12.46
5BZB J1004+3752	J1004.4+3750	3.09	3.09	0.00	-0.01	9.75
5BZB J1207-1746	J1207.0-1746	0.00	7.58	0.09	0.09	10.83
5BZG J0643+4214	J0643.4+4215	0.00	2.14	2.40	3.99	6.16
5BZB J0742+3018	J0742.9+3021	0.00	-0.01	2.89	2.29	9.56
5BZB J0250-2129	J0250.4-2130	0.00	0.48	0.00	0.00	11.88
5BZQ J1215+3448	J1216.2+3451	0.00	2.16	2.30	3.72	8.95
5BZQ J1220+0203	J1219.9+0200	0.00	0.12	1.08	0.81	1.73
5BZQ J1342-2900	J1342.3-2901	7.87	5.67	3.24	1.11	0.68
5BZQ J1012+2312	J1012.0+2313	0.00	6.15	0.05	1.51	16.94
5BZB J1337+0035	J1336.8+0040	0.00	4.33	0.00	0.00	5.34
5BZQ J1044+5322	J1043.7+5323	0.00	0.84	0.00	0.00	267.85
5BZG J1531+0852	J1531.7+0845	0.00	0.00	0.00	0.00	11.11
5BZQ J0756-1542	J0756.6-1534	0.00	0.00	0.00	0.00	24.73
5BZQ J1243+4043	J1243.9+4046	0.00	1.23	-0.01	-0.01	14.08
5BZQ J0205+1444	J0205.4+1441	0.00	0.09	0.18	0.14	19.29

Note. This table summarizes the spectral, spatial, and temporal variability analysis results for 17 newly identified GeV blazars. TS_{cur,lp} and TS_{cur,plec} represent the spectral curvature indices derived from the LP and PLEC models, respectively. TS_{ext,Disk} and TS_{ext,Gauss} represent the spatial extension test statistics obtained using the uniform disk and 2D-Gaussian models, respectively. TS_{var} indicates the variability index derived from the light curve analysis with a 1-year time binning.

commonly known as the “blazar dichotomy”. Although a general consensus exists within the astronomical community regarding the differences between BZBs and BZQs, several key questions remain unresolved. These questions include:

- (i) To what extent do the flux distributions between BZBs and BZQs differ statistically across different energy bands?
- (ii) How can such differences be comprehensively and accurately quantified?
- (iii) What physical mechanisms drive the differences between their distributions?

As one of the most fundamental observable physical quantities, flux is not only closely related to key parameters such as luminosity, magnitude, and redshift, but is also strongly linked to the radiation mechanisms, jet formation processes, and beaming effects of blazars, as elaborated in Section 3.1. This makes flux an ideal physical probe, whose statistical behavior can effectively reveal the underlying physical processes of blazars. Moreover, the extensive availability of flux measurements across diverse observational catalogs offers a crucial data foundation for conducting large-sample statistical analyses of blazar flux distributions. The 5BZCAT_err is a large and well-classified blazar catalog, providing an ideal sample basis for this study. Conducting a systematic statistical analysis of its multi-band flux distributions carries the following significant scientific implications:

- (a) To provide key observational evidence for systematically revealing the fundamental differences between BZBs and BZQs in their multi-band energy output and radiation mechanisms.
- (b) By precisely quantifying the differences in these flux distributions, this study will provide key observational constraints on the radiation mechanisms and particle acceleration processes of these two subclasses, and offer new supporting evidence for the blazar dichotomy.

- (c) To explore and construct new classification criteria based on multi-band flux statistical distributions, in order to establish a more robust classification paradigm that overcomes the traditional over-reliance on single, variable optical spectral observations, thereby improving classification accuracy and reliability. In addition, this new paradigm can serve as a tool for identifying new blazars in large samples, especially when classification features are ambiguous.

Therefore, our core motivation is to quantitatively characterize and compare the multi-band flux distribution features of BZBs and BZQs. We aim to answer the following questions:

- (1) What are the characteristics of the flux distributions for BZBs and BZQs in different energy bands?
- (2) Are the distributional characteristics of BZBs and BZQs significantly different, and how can we comprehensively quantify the degree of this difference?
- (3) Can we construct a unified distribution model that characterizes the flux distributions of BZBs and BZQs, which could then serve as a new criterion for identifying new candidates of these subclasses?

To address the above issues, we will describe our research pipeline sequentially in the following three subsections (Sections 2.6.1 to 2.6.2).

2.6.1. Investigating the differences in multi-Wavelength flux distributions Between BZBs and BZQs

To ensure comprehensive spectral coverage and sufficient observational data, this study selected flux measurements spanning from radio to γ -ray bands as the targets of analysis. Specifically, fluxes at 74 MHz, 365 MHz, 843 MHz, 1.4 GHz, 5 GHz, 15 GHz, 20 GHz, 143 GHz, 0.1–2.4 keV, 0.3–10 keV, and 0.1–100 GeV were included. To systematically investigate the statistical properties of blazar fluxes across multiple wavebands, we selected the 5BZCAT_err sample for analysis and designed a standardized data extraction procedure. Following the corresponding technical pipeline illustrated in Appendix C.1, we successfully retrieved multi-wavelength flux data for 3,442 sources in the aforementioned spectral bands.

To investigate the similarities and differences in the multi-wavelength flux distributions of BZBs and BZQs, we have designed a specialized analysis pipeline aimed at in-depth statistical characterization (see Appendix C.2 for detailed procedures and data). We first performed a logarithmic transformation on the flux data of the 5BZCAT_err blazars and calculated eight common statistical parameters, such as the mean, median, skewness, and kurtosis, to comprehensively characterize their distribution properties. Subsequently, we introduced the Median Absolute Deviation (MAD) to quantify the degree of difference in various statistical indicators across different bands. Based on this, we analyzed the similarities and differences between BZBs and BZQs in terms of their distribution center, dispersion, and shape. The MAD analysis results show that BZBs and BZQs exhibit varying degrees of statistical differences in their multi-wavelength flux distributions, with the difference in kurtosis being the most prominent ($MAD = 1.64$).

In addition to using MAD analysis to assess differences in statistical parameters, this study also introduces the Jensen-Shannon distance (JSD) as a supplementary metric to evaluate the differences between BZBs and BZQs in their overall multi-wavelength flux distribution characteristics. The JSD is capable of assessing the overall difference between two distributions based on their probability density distributions (PDDs). JSD analysis reveals that the flux distribution differences between BZBs and BZQs are most prominent in the 1.4 GHz and 0.1–2.4 keV bands ($JSD > 0.3$). In other bands, although the differences are relatively smaller, the JSD values remain positive, indicating that the two source types exhibit systematic distributional differences of varying degrees across all bands.

In summary, both the MAD values of the eight classical statistical indicators and the JSD analysis results are consistently greater than zero, providing strong evidence that BZBs and BZQs exhibit systematic differences in their flux distributions.

2.6.2. Modeling multi-band flux distributions via Box-Cox transformation and truncated normal distributions

According to the analysis in Section 2.6.1, the flux distributions of BZQs and BZBs show varying degrees of divergence across the radio to γ -ray bands, with kurtosis emerging as the most discriminative statistical metric. The flux kurtosis of BZQs is consistently higher than that of BZBs across all wavebands, with the most significant difference occurring at 143 GHz. However, employing kurtosis at 143 GHz as a classification criterion for blazars presents two key challenges:

- (1) Although higher kurtosis values were observed in the 143 GHz band, it is important to note that the sample size in this band is extremely limited, with only 8 data points for BZBs and 50 for BZQs. Given such a small sample, the estimation of the distributional characteristics of BZBs is likely subject to considerable statistical uncertainty. Moreover, kurtosis captures only a single aspect of a distribution and cannot comprehensively characterize its overall

characteristics. Therefore, relying on the kurtosis at 143 GHz as a classification criterion for BZBs and BZQs is not statistically robust.

(2) Except for the 143 GHz band, differences in flux distributions across other wavebands are not taken into account. Relying solely on a single-band criterion is insufficient to fully characterize the multi-band radiative properties arising from the jets and accretion disks of BZBs and BZQs.

In summary, to evaluate the common statistical characteristics of the multi-band fluxes of the 17 new GeV blazars and the 5BZCAT_err sample, and to provide robust statistical support for classification and identification, two key issues should be addressed:

- (a) The limitations of using single-band criteria for classification;
- (b) The lack of a unified statistical model and reliable indicators for quantifying the shared characteristics of flux distributions.

To address the first problem, we adopted an approach that focuses on commonly available multi-band flux data, thereby avoiding the limitations of relying on single-waveband criteria for classification and identification.

To address the second problem, we designed a statistical modeling approach that combines the Box–Cox transformation with the truncated normal distribution (TND) to systematically characterize the multi-band flux distributions of BZBs and BZQs. To achieve a unified modeling of multi-band flux distributions, we propose a statistical method that combines the Box-Cox transformation and the Truncated Normal Distribution (TND). The procedure first applies the Box-Cox transformation to normalize the data, and then fits the data with the TND model. The goodness-of-fit is evaluated using the Kolmogorov-Smirnov (KS) test, with a requirement of $p > 0.05$. The analysis reveals that the BZQ sample at 74 MHz did not initially pass the KS test due to the presence of outliers. To address this, we applied the Local Outlier Factor (LOF) algorithm to remove a few outliers, after which the corrected data successfully passed the test. Notably, the data from all other bands met the fitting criteria without requiring additional processing. This result confirms the general applicability and robustness of our proposed “Box-Cox + TND” model. The complete details of this modeling procedure are provided in Appendix C.3.

2.6.3. Application of the model

In Section 2.1, data analysis was performed for the 100 MeV to 1 TeV energy band, yielding the corresponding photon flux. However, in Section 2.6.1, the high-energy band for blazars is defined as 100 MeV to 100 GeV. To maintain consistency in the energy range, **Fermipy** was employed to recalculate the photon flux for the 17 blazar candidates within the 100 MeV to 100 GeV band, in preparation for subsequent statistical analysis. Then, based on the Box–Cox transformation parameters λ listed in Table 11, we uniformly transformed the flux values of the 17 blazar candidates across each observational waveband using Equation C5.

The resulting Box–Cox transformed values are plotted on the optimal TND fitting curves corresponding to each waveband and source type, facilitating an intuitive comparison of the relative positions of each candidate within the overall distribution. Using 5BZQ J1220+0203 as an example, we present the statistical analysis results of its multi-band flux distribution in Figure 5, with the transformed data points annotated on the optimal fitted curve to highlight their positions relative to the 1σ and 2σ confidence intervals (CIs). Similar plots for the remaining 16 candidates are included in the archive `Model_fitting_results.tar.xz`, as referenced in Section 5. The corresponding z-score statistics for each candidate are summarized in Table 4.

Based on the z-score analysis of 5BZQ J1220+0203 across six wavebands, the source shows flux levels exceeding the mean of the larger BZQ sample in the 74 MHz, 1.4 GHz, and 0.1–2.4 keV bands, as evidenced by positive z-scores. Conversely, in the 365 MHz, 5 GHz, and 0.1–100 GeV bands, negative z-scores indicate that the source’s flux falls below the respective mean. Further examination revealed that the transformed fluxes in the four bands—74 MHz, 365 MHz, 1.4 GHz, and 5 GHz—all lie within the 1σ CI of the modeled distribution. This indicates that, in these wavebands, the flux of 5BZQ J1220+0203 is relatively typical and shows no significant deviations. In the 0.1–2.4 keV and 0.1–100 GeV bands, the transformed fluxes lie within the 2σ CI of the modeled distribution, suggesting moderate deviations that nonetheless remain within a statistically acceptable range. This indicates that the radiation characteristics of 5BZQ J1220+0203 in these wavebands exhibit strong similarity to those observed in larger samples. As discussed in Section 3.1, the differences in multi-band flux distributions between BZBs and BZQs are highly likely governed by redshift and three physical mechanisms. Therefore, we speculate that 5BZQ J1220+0203 likely shares similar intrinsic properties and emission behaviors with the larger BZQ population.

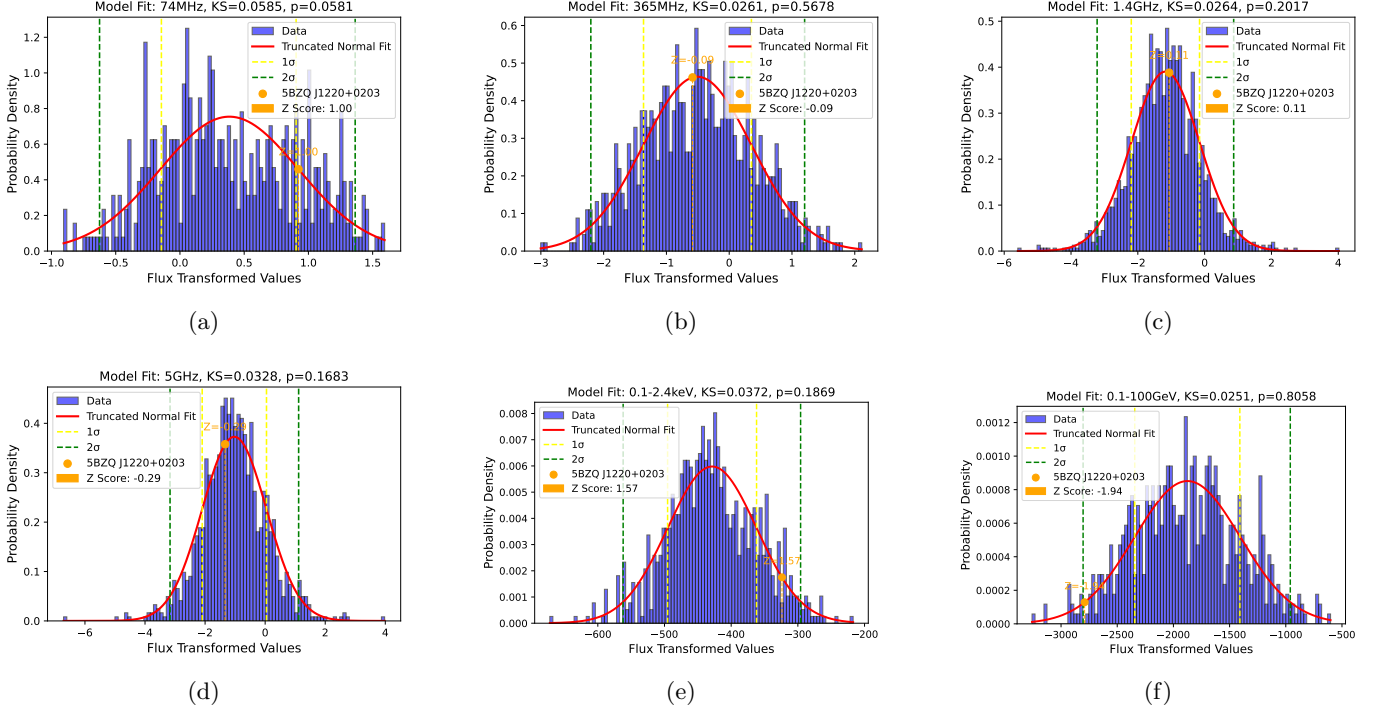


Figure 5. The figure displays the flux distribution analysis results for 5BZQ J1220+0203 across the 74 MHz, 365 MHz, 1.4 GHz, 5 GHz, 0.1–2.4 keV, and 0.1–100 GeV bands. The blue histogram depicts the density distribution of Box-Cox transformed flux values from a large sample, while the red curve represents the best-fit TND. Yellow dashed lines denote the 1σ CI, and green dashed lines indicate the 2σ CI. The orange point marks the position of 5BZQ J1220+0203, accompanied by its annotated z-score value.

Table 4. Results of Statistical Analysis for 17 New GeV Blazars

Name	Waveband	Type	Box–Cox Flux	CI	Z-score
5BZQ J1215+3448	74 MHz	BZQ	0.943	2σ	1.034
5BZQ J1215+3448	365 MHz	BZQ	0.720	2σ	1.422
5BZQ J1215+3448	1.4 GHz	BZQ	0.346	2σ	1.488
5BZQ J1215+3448	5 GHz	BZQ	-0.314	1σ	0.665
5BZQ J1215+3448	0.1–2.4 keV	BZQ	-471.867	1σ	-0.648
5BZQ J1215+3448	0.1–100 GeV	BZQ	-3013.069	$> 2\sigma$	-2.417
5BZQ J1220+0203	74 MHz	BZQ	0.923	1σ	0.997
5BZQ J1220+0203	365 MHz	BZQ	-0.584	1σ	-0.089
5BZQ J1220+0203	1.4 GHz	BZQ	-1.062	1σ	0.110
5BZQ J1220+0203	5 GHz	BZQ	-1.334	1σ	-0.288
5BZQ J1220+0203	0.1–2.4 keV	BZQ	-323.834	2σ	1.568
5BZQ J1220+0203	0.1–100 GeV	BZQ	-2790.174	2σ	-1.944
5BZQ J1342-2900	365 MHz	BZQ	-1.560	2σ	-1.220
5BZQ J1342-2900	1.4 GHz	BZQ	-1.140	1σ	0.034
5BZQ J1342-2900	5 GHz	BZQ	-0.853	1σ	0.162
5BZQ J1342-2900	20 GHz	BZQ	-0.855	1σ	0.427
5BZQ J1342-2900	0.1–100 GeV	BZQ	-2774.527	2σ	-1.910
5BZQ J1012+2312	1.4 GHz	BZQ	-1.808	1σ	-0.620
5BZQ J1012+2312	5 GHz	BZQ	-1.273	1σ	-0.231
5BZQ J1012+2312	15 GHz	BZQ	-1.264	1σ	-0.104

Name	Waveband	Type	Box–Cox Flux	CI	Z-score
5BZQ J1012+2312	0.1-2.4 keV	BZQ	-440.011	1σ	-0.172
5BZQ J1012+2312	0.3-10 keV	BZQ	-97.289	1σ	-0.360
5BZQ J1012+2312	0.1-100 GeV	BZQ	-2690.863	2σ	-1.733
5BZQ J0756-1542	74 MHz	BZQ	0.561	1σ	0.327
5BZQ J0756-1542	365 MHz	BZQ	-0.075	1σ	0.501
5BZQ J0756-1542	1.4 GHz	BZQ	-0.180	1σ	0.974
5BZQ J0756-1542	5 GHz	BZQ	0.150	2σ	1.098
5BZQ J0756-1542	20 GHz	BZQ	-0.332	1σ	0.865
5BZQ J0756-1542	0.1-100 GeV	BZQ	-2230.560	1σ	-0.756
5BZB J1411+3404	0.1-2.4 keV	BZB	-37.816	1σ	-0.894
5BZB J1411+3404	0.1-100 GeV	BZB	-3310.612	2σ	-1.794
5BZB J1221+0821	365 MHz	BZB	-1.401	1σ	-0.836
5BZB J1221+0821	1.4 GHz	BZB	-1.826	1σ	0.798
5BZB J1221+0821	5 GHz	BZB	-3.418	1σ	-0.981
5BZB J1221+0821	0.1-2.4 keV	BZB	-36.161	1σ	-0.234
5BZB J1221+0821	0.1-100 GeV	BZB	-2854.699	2σ	-1.004
5BZB J1004+3752	1.4 GHz	BZB	-3.300	1σ	-0.037
5BZB J1004+3752	0.1-2.4 keV	BZB	-37.332	1σ	-0.701
5BZB J1004+3752	0.1-100 GeV	BZB	-3299.560	2σ	-1.775
5BZB J1207-1746	1.4 GHz	BZB	-6.399	2σ	-1.793
5BZB J1207-1746	0.1-2.4 keV	BZB	-33.848	1σ	0.687
5BZB J1207-1746	0.1-100 GeV	BZB	-2814.007	1σ	-0.933
5BZB J0643+4214	5 GHz	BZB	-3.327	1σ	-0.917
5BZB J0643+4214	0.1-2.4 keV	BZB	-32.470	2σ	1.236
5BZB J0643+4214	0.1-100 GeV	BZB	-3174.972	2σ	-1.559
5BZB J0742+3018	1.4 GHz	BZB	-4.149	1σ	-0.518
5BZB J0742+3018	0.1-100 GeV	BZB	-2987.876	2σ	-1.235
5BZB J0250-2129	0.1-2.4 keV	BZB	-34.047	1σ	0.608
5BZB J0250-2129	0.1-100 GeV	BZB	-3341.606	2σ	-1.848
5BZQ J1243+4043	1.4 GHz	BZQ	-1.570	1σ	-0.387
5BZQ J1243+4043	5 GHz	BZQ	-1.758	1σ	-0.684
5BZQ J1243+4043	0.1-100 GeV	BZQ	-3293.402	$\geq 2\sigma$	-3.012
5BZB J1337+0035	1.4 GHz	BZB	-2.133	1σ	0.625
5BZB J1337+0035	0.1-2.4 keV	BZB	-38.838	2σ	-1.301
5BZB J1337+0035	0.1-100 GeV	BZB	-3051.207	2σ	-1.344
5BZQ J1044+5322	365 MHz	BZQ	-0.810	1σ	-0.352
5BZQ J1044+5322	1.4 GHz	BZQ	-0.846	1σ	0.321
5BZQ J1044+5322	5 GHz	BZQ	-1.181	1σ	-0.145
5BZQ J1044+5322	15 GHz	BZQ	-1.334	1σ	-0.162
5BZQ J1044+5322	0.1-2.4 keV	BZQ	-445.018	1σ	-0.246
5BZQ J1044+5322	0.1-100 GeV	BZQ	-2053.905	1σ	-0.380
5BZB J1531+0852	0.1-100 GeV	BZB	-3048.081	2σ	-1.339
5BZQ J0205+1444	1.4 GHz	BZQ	-1.540	1σ	-0.358
5BZQ J0205+1444	0.1-100 GeV	BZQ	-2736.900	2σ	-1.830

Note. Please refer to Table 6 for keyword explanations and units.

3. DISCUSSION

3.1. Exploring the Likely Physical Origins of Differences in Multi-Wavelength Flux Distribution Between BZBs and BZQs

The statistical differences observed in the multi-wavelength flux distributions between BZBs and BZQs likely stem from fundamental distinctions in their underlying physical properties, such as radiation mechanisms, jet formation processes, and relativistic beaming effects. In the following sections, we provide a comprehensive analysis of the intrinsic relationships between these physical mechanisms and the multi-wavelength flux characteristics of BZBs and BZQs.

(1) Different Radiation Mechanisms

Studies by [M. Böttcher et al. \(2013\)](#) and [A. Abdo et al. \(2010b\)](#) indicate that the leptonic model effectively explains the quasi-simultaneous SEDs of most blazars in the high-energy band, thereby offering strong support for the hypothesis that their high-energy emission stems from leptonic processes. Within the framework of leptonic models, different radiation mechanisms dominate at various frequency bands. For BZBs, the emission from radio to X-ray bands is primarily produced by synchrotron radiation from relativistic electrons in the jet's magnetic field, while their SEDs in the GeV to TeV band are typically dominated by the SSC process. In contrast, BZQs often exhibit prominent EC components, resulting from the scattering of external photon fields—such as those originating from the BLR or the dusty torus—by relativistic electrons. The dominance of EC processes not only contributes significantly to the low-frequency emission but also enhances the high-energy component and shifts the peak frequency of their SEDs to lower values ([G. a. Fossati et al. 1998](#); [G. Ghisellini et al. 1998](#); [M. Böttcher et al. 2013](#); [J. Fan et al. 2016](#)). Systematic differences in radiation mechanisms are likely to result in variations in the $\nu_{\text{peak}}^{\text{S}}$. The study by [A. Abdo et al. \(2010b\)](#) provides robust evidence in support of this inference.

Through a comprehensive analysis of the multi-wavelength radiation properties of 48 bright γ -ray blazars observed by Fermi-LAT, they demonstrated that the distributions of $\nu_{\text{peak}}^{\text{S}}$ differ significantly between BZBs and BZQs. To provide stronger statistical support for this difference, we first extracted the $\log(\nu_{\text{peak}}^{\text{S}})$ data from Table 13 of [A. Abdo et al. \(2010b\)](#) and constructed histograms of the $\log(\nu_{\text{peak}}^{\text{S}})$ for both BZBs and BZQs. As shown in Figure 6, a clear distinction is observed in their distribution characteristics: the peak frequencies of BZQs are primarily concentrated in the lower-frequency range with a relatively narrow spread, whereas those of BZBs exhibit a broader range and are generally shifted toward higher frequencies.

Table 5. Statistical Comparison of Physical Properties between BZBs and BZQs

Sample	Min	Max	Mean	Median	Mode	Std	Skewness	Kurtosis	JSD
$\log \nu_{\text{peak,BZB}}^{\text{S}}$ vs $\log \nu_{\text{peak,BZQ}}^{\text{S}}$									
$\log \nu_{\text{peak,BZB}}^{\text{S}}$	12.6	16.5	14.58	14.5	13.8	0.97	0.21	-0.79	0.56
$\log \nu_{\text{peak,BZQ}}^{\text{S}}$	12.4	14.8	13.16	13.1	13.0	0.42	0.98	2.53	
$\log P_{\text{jet,BZ,BZB}}$ vs $\log P_{\text{jet,BP,BZQ}}$									
$\log P_{\text{jet,BZ,BZB}}$	43.17	46.86	44.52	44.48	44.34	0.58	0.67	1.39	0.67
$\log P_{\text{jet,BP,BZQ}}$	41.08	49.17	46.67	46.85	46.85	1.15	-1.21	2.56	
$\log R_{\text{v,BZB}}$ vs $\log R_{\text{v,BZQ}}$									
$\log R_{\text{v,BZB}}$	0.15	3.99	2.23	2.15	0.15	0.81	0.01	-0.16	0.51
$\log R_{\text{v,BZQ}}$	1.90	4.83	3.51	3.57	1.90	0.60	-0.47	-0.19	
z_{BZB} vs z_{BZQ}									
z_{BZB}	0.00	3.53	0.42	0.31	0.70	0.39	2.68	10.66	0.48
z_{BZQ}	0.03	4.31	1.19	1.11	0.72	0.66	0.81	0.86	

Subsequently, we conducted a comparative analysis following the technical procedure outlined in Content 4 of Figure 17. As shown in Table 5, BZBs exhibit significantly higher values of $\nu_{\text{peak}}^{\text{S}}$ than BZQs, characterized by a broader distribution range (min = 12.6, max = 16.5) and a higher mean value (14.58 for BZBs vs. 13.16 for BZQs).

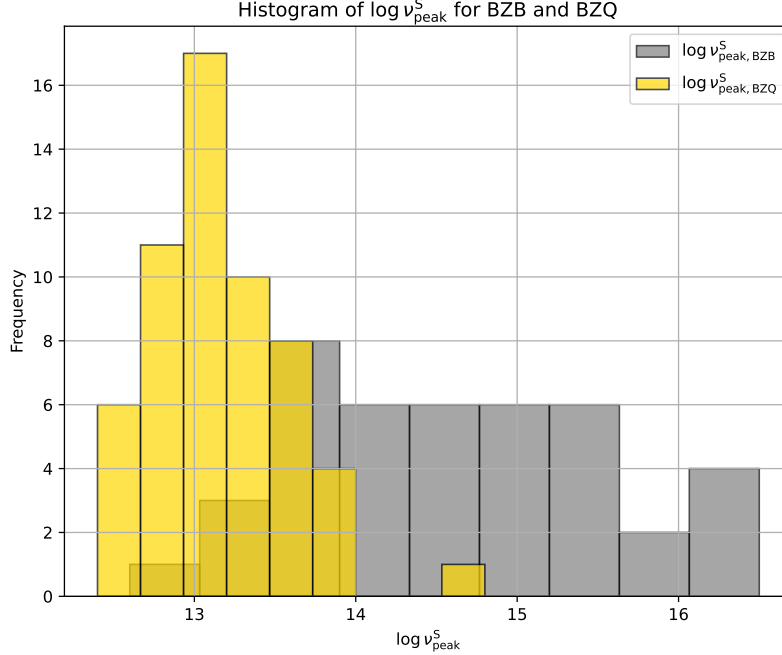


Figure 6. This figure shows the distributions of $\log \nu_{\text{peak},\text{BZB}}^S$ and $\log \nu_{\text{peak},\text{BZQ}}^S$, representing the synchrotron peak frequencies of BZBs and BZQs, shown in grey and yellow, respectively.

The std of $\log \nu_{\text{peak},\text{BZB}}^S$ distribution (std = 0.97) is more than approximately twice that of $\log \nu_{\text{peak},\text{BZQ}}^S$ (std = 0.42), indicating substantially greater dispersion. Moreover, the skewness and kurtosis values suggest that $\log \nu_{\text{peak},\text{BZB}}^S$ distribution is more symmetric and flatter, while that of BZQs displays strong positive skewness (Skewness = 0.98) and a sharply peaked distribution (Kurtosis = 2.53). Meanwhile, the JSD value of 0.56 further confirms the significant difference between the $\log(\nu_{\text{peak}}^S)$ distributions between BZBs and BZQs from the perspective of the overall probability density profiles.

Based on the above analysis, we suggest that differences in the underlying radiation mechanisms play a key role in producing the differences observed in the multi-band SEDs, thereby influencing the distribution characteristics of the $\log(\nu_{\text{peak}}^S)$. The significant discrepancy between $\log \nu_{\text{peak},\text{BZB}}^S$ and $\log \nu_{\text{peak},\text{BZQ}}^S$ likely contributes to the differences observed in the flux distributions at specific bands, such as 1.4 GHz and 0.1–2.4 keV, and other wavebands.

(2) Different Jet Formation Mechanisms

Currently, two mainstream models are widely accepted to explain the formation of blazar jets: the Blandford–Znajek (BZ) and Blandford–Payne (BP) models. In the BZ model, the jet is powered by the rotational energy of the black hole, with its energy output governed by both the spin and mass of the black hole (R. D. Blandford & R. L. Znajek 1977). In contrast, the BP model drives the jet by extracting energy from the rotational motion of the accretion disk (R. D. Blandford & D. Payne 1982). Based on the analysis of the relationship between jet power and normalized disk luminosity, H. Xiao et al. (2022) suggested that the jets of BL Lacs are more likely powered by black hole spin, consistent with the BZ mechanism, where jet energy is extracted through the interaction between a rotating black hole and its magnetic field. In contrast, the jets of BZQs are more likely driven by the rotational energy of the accretion disk, consistent with the BP mechanism, in which magnetic field lines anchored in the disk extract and accelerate material to form jets (H. Xiao et al. 2022). Furthermore, S. Xie et al. (2024) found that the jet powers of BZQs, as estimated from radio flux density, closely match the theoretical predictions of the BP mechanism, whereas those of BZBs are more consistent with the expectations of the BZ mechanism. This finding further highlights that BZBs and BZQs differ markedly in their jet formation mechanisms.

To further quantify the impact of the BZ and BP mechanisms on the jet power of the two blazar subclasses, we extracted the relevant data from Table 3 of S. Xie et al. (2024) and constructed the frequency histograms shown in Figure 7 to visualize the distribution characteristics of jet power for each class. Additionally, we performed a quantitative analysis of the two distributions following the methodology outlined in Content 4 of Figure 17. The

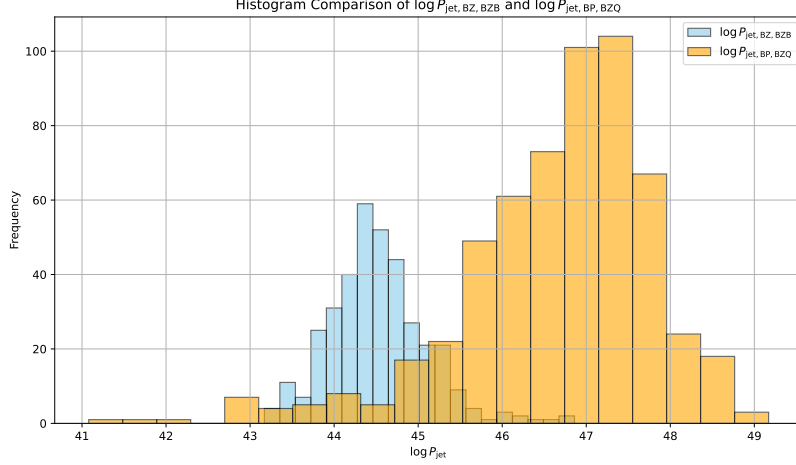


Figure 7. This figure presents the distributions of $\log P_{\text{jet,BZ,BZB}}$ and $\log P_{\text{jet,BP,BZQ}}$, where $P_{\text{jet,BZ,BZB}}$ represents the jet power derived from the BZ model for BZBs, depicted in blue, and $P_{\text{jet,BP,BZQ}}$ represents the jet power derived from the BP model for BZQs, depicted in orange.

results, summarized in Table 5, reveal significant differences in the jet power ($\log P_{\text{jet}}$) distributions between BZBs and BZQs. These differences are evident in several key statistical characteristics, as detailed below:

First, in terms of central tendency, the mean and median of $\log P_{\text{jet,BZ,BZB}}$ distribution are 44.52 and 44.48, respectively, while those of $\log P_{\text{jet,BP,BZQ}}$ distribution are 46.67 and 46.85. This reflects a difference of approximately two orders of magnitude, suggesting that BZQs generally exhibit significantly higher jet power than BZBs.

Second, with respect to std, BZBs show a value of 0.59, while BZQs reach 1.15, indicating that the jet power distribution for BZQs is more dispersed and covers a broader energy range. Furthermore, regarding skewness, BZBs display a slight positive skew with a skewness value of 0.66, whereas BZQs show a significant negative skew of -1.21. This suggests that BZBs are mainly concentrated in the lower-power regime, while BZQs include a larger proportion of high-power sources. In addition, the kurtosis of BZQs is 2.55, higher than the value of 1.39 observed for BZBs, indicating that the jet power distribution of BZQs is more sharply peaked and exhibits a higher likelihood of extreme values. The JSD value of 0.67 quantifies the difference between the PDDs of $\log P_{\text{jet,BZ,BZB}}$ and $\log P_{\text{jet,BP,BZQ}}$, revealing a significant overall discrepancy. As shown in Figure 7, the jet power distributions of BZBs and BZQs exhibit marked differences: BZQs display a significantly higher distribution peak, a broader range, and a sharper profile, while BZBs display a more concentrated distribution skewed toward the lower-power regime.

According to the empirical formula (1) proposed by L. Foschini et al. (2024) and S. Xie et al. (2024), derived from the R. Blandford & A. Königl (1979) model,

$$P_{\text{jet}} = (4.5 \times 10^{44}) \left(\frac{S_{\text{obs}} d_{L,9}^2}{1+z} \right)^{\frac{12}{17}} \quad (1)$$

the relationship between the jet power P_{jet} and observed flux S_{obs} indicates that systematic differences in jet power between BZBs and BZQs are likely a key factor contributing to the observed discrepancies in their flux distributions.

In summary, differences in jet formation mechanisms likely result in variations in the jet power distributions between BZBs and BZQs. Via the coupling relationship between jet power and flux described in Equation 1, these variations are likely to further contribute to the statistical differences observed in their multi-wavelength flux distributions.

(3) Difference in Doppler boosting effect

The Doppler beaming effect is a key factor explaining why blazars display rapid variability, high luminosity, and strong, variable polarization (C. M. Urry & P. Padovani 1995; J. Fan et al. 2017; W. Yang et al. 2022). Its macroscopic manifestation is Doppler boosting, which refers to the apparent enhancement of radiation toward the observer due to the relativistic motion of a jet approaching the speed of light (C. M. Urry & P. Padovani 1995; D.-C. Mei et al. 1999; J. Zhou & Y. Su 2006; R. Capdessus et al. 2018). To quantify the strength of this effect, B. J. Wills & M. Brotherton

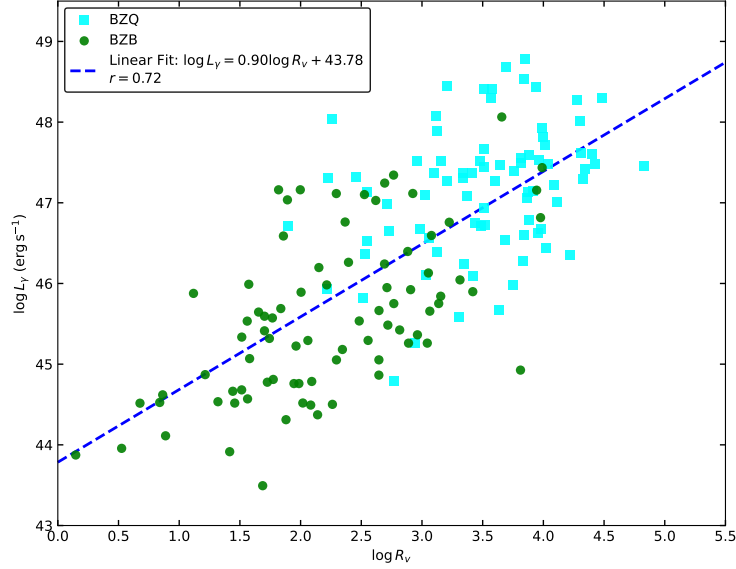


Figure 8. The relationship between the logarithmic beaming factor $\log R_v$ and the logarithmic γ -ray luminosity $\log L_\gamma$ is depicted, with cyan points denoting BZQs, green points denoting BZBs, and the blue dashed line representing the best-fit curve derived from Equation 4. The Pearson correlation coefficient is indicated by r .

(1995) introduced a robust and widely used parameter—the beaming factor R_v , defined as the ratio of the radio core luminosity to the optical continuum luminosity in the V band. The formula is given by:

$$\log R_v = \log \left(\frac{L_{\text{core}}}{L_{\text{opt}}} \right) = \log L_{\text{core}} + \frac{M_{\text{abs}}}{2.5} - 13.7 \quad (2)$$

In Equation 2, L_{core} denotes the radio core luminosity, and L_{opt} represents the optical continuum luminosity in the V band. The absolute optical magnitude with k-correction, M_{abs} , is defined as $M_{\text{abs}} = M_V - k$, where M_V is the apparent magnitude in the V band, and the k-correction term k is given by:

$$k = -2.5 \log(1 + z)^{1 - \alpha_{\text{opt}}} \quad (3)$$

A typical value of the optical spectral index is assumed to be $\alpha_{\text{opt}} = 0.5$. A higher R_v value generally indicates that the jet is more aligned with the observer’s line of sight, implying a stronger Doppler boosting effect.

In a study utilizing the 3FGL sample, Y.-Y. Chen et al. (2016) examined the relationship between R_v and the γ -ray luminosity L_γ for BZBs and BZQs, revealing a statistically significant positive correlation between $\log R_v$ and $\log L_\gamma$. For the full blazar sample, a Pearson correlation coefficient of 0.72 indicates a strong linear relationship between the two physical quantities. Based on this, we extracted the pertinent $\log R_v$ and $\log L_\gamma$ data from Y.-Y. Chen et al. (2016) to further examine the linear correlation between these two variables. Assuming that $\log L_\gamma$ and $\log R_v$ adhere to the linear relationship outlined in Equation 4, we conducted a linear regression analysis employing the `LinearRegression` class from the `scikit-learn` machine learning library (F. Pedregosa et al. 2011). The optimal parameters a and b were determined to be 0.90 and 43.78, respectively.

$$\log L_\gamma = a \log R_v + b \quad (4)$$

Subsequently, we utilized the `pearsonr` function from the `SciPy` statistics module (P. Virtanen et al. 2020) to compute the Pearson correlation coefficient between the two variables, obtaining a value of 0.72, consistent with the findings reported by Y.-Y. Chen et al. (2016). The correlation fitting results, as shown in Figure 8, indicate that Equation 4 adequately accounts for the linear relationship between the two variables. Additionally, the data reveal distinct trends for BZBs and BZQs: $\log R_{v,\text{BZB}}$ values are mainly clustered in the lower-left region, while $\log R_{v,\text{BZQ}}$ values are predominantly situated in the upper-right region.

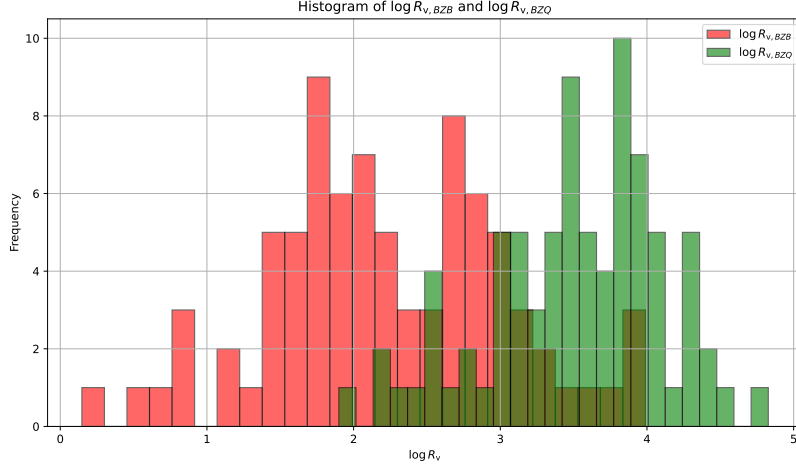


Figure 9. This figure displays the distributions of $\log R_{v,BZB}$ and $\log R_{v,BZQ}$, representing the logarithmic beaming factors of BZBs and BZQs, respectively. The red histogram represents the distribution of $\log R_{v,BZB}$, while the green histogram depicts that of $\log R_{v,BZQ}$.

Following the methodology detailed in Content 3 of Figure 17, we conducted a systematic evaluation of the distributional differences in $\log R_v$ between BZBs and BZQs. Specifically, we generated frequency histograms for each subclass based on their respective $\log R_v$ values. As shown in Figure 9, the $\log R_v$ distributions for BZBs and BZQs display marked differences. The $\log R_{v,BZB}$ values are mainly concentrated in the lower range, whereas the $\log R_{v,BZQ}$ distribution is notably shifted toward higher values. Moreover, as evidenced by the analytical results in Table 5, BZBs and BZQs exhibit systematic differences in the distributional characteristics of $\log R_v$. Both the mean and median values of $\log R_{v,BZQ}$ are markedly higher than those of $\log R_{v,BZB}$, indicating that BZQs generally exhibit stronger Doppler beaming effects than BZBs. Furthermore, the range of $\log R_{v,BZQ}$, spanning 1.90 to 4.83, is almost entirely greater than that of $\log R_{v,BZB}$, which extends from 0.15 to 3.99. The limited overlap between the two distributions underscores a clear separation between BZBs and BZQs. Moreover, the std of $\log R_{v,BZB}$ is 0.81, exceeding that of $\log R_{v,BZQ}$ at 0.60. This indicates that the $\log R_{v,BZB}$ distribution is more dispersed, reflecting greater variability among individual sources, whereas the $\log R_{v,BZQ}$ values are more tightly clustered. Skewness analysis reveals that the distribution of $\log R_{v,BZB}$ is approximately symmetric, with a skewness of 0.01, whereas $\log R_{v,BZQ}$ exhibits a slight negative skew with a skewness of -0.47, indicating a concentration of $\log R_{v,BZQ}$ values toward higher ranges. Both source classes exhibit negative kurtosis values, with $\log R_{v,BZB}$ at -0.16 and $\log R_{v,BZQ}$ at -0.19, indicating that their distributions are flatter than the SND. The JSD value of 0.51 quantifies the distinction of the PDDs between $\log R_{v,BZB}$ and $\log R_{v,BZQ}$, revealing a significant difference in their overall distributional characteristics.

For blazars, the luminosity L in a specific waveband and the flux S satisfy the following relationship:

$$L = 4\pi d_L^2 S \quad (5)$$

where d_L is the luminosity distance, S needs to be corrected for redshift using the k-correction, given by:

$$S = S_{\text{obs}}(1+z)^{\alpha-1} \quad (6)$$

where z is the redshift and α is the spectral index. Drawing from Equations 2, 4, and 5, we infer the existence of a coupling relationship between R_v and the flux spanning the radio to γ -ray bands. This suggests that the difference in jet beaming effects between BZBs and BZQs is likely an important factor contributing to the observed differences in their flux distributions.

(4) Different Redshift distributions

Redshift (z), as an observable quantity reflecting a source's relative motion or cosmological distance from us (W. L. Freedman & B. F. Madore 2010), is inextricably linked to the magnitude of the observed flux. After light is emitted from a source, it propagates in all directions. As distance increases, the light spreads over a larger spherical surface, so the number of photons received per unit area decreases. This follows the famous inverse square law. Light from

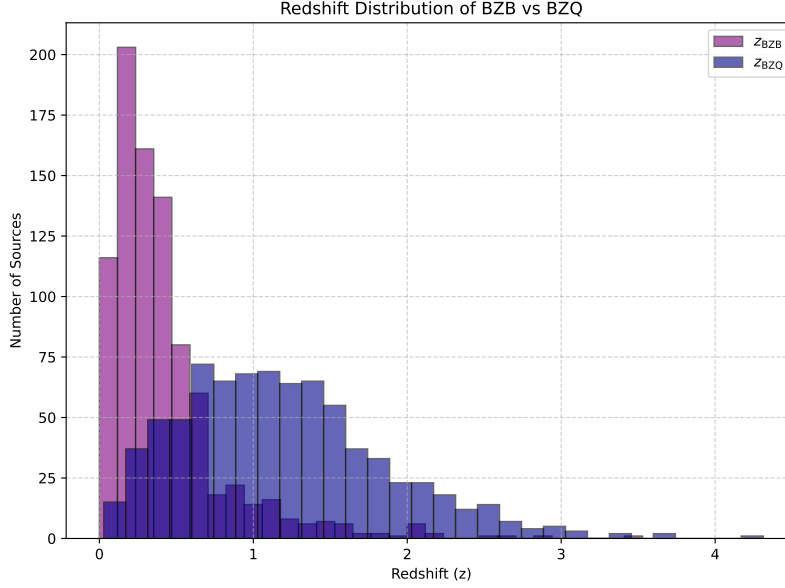


Figure 10. This figure presents the distributions of $\log P_{\text{jet,BZ,BZB}}$ and $\log P_{\text{jet,BP,BZQ}}$, where $P_{\text{jet,BZ,BZB}}$ represents the jet power derived from the BZ model for BZBs, depicted in blue, and $P_{\text{jet,BP,BZQ}}$ represents the jet power derived from the BP model for BZQs, depicted in orange.

a source radiates outwards in all directions. As the distance of the source increases, this light spreads over a larger spherical area, causing the flux (the number of photons per unit area) to decrease. This relationship is known as the inverse square law¹⁰. Secondly, due to the expansion of the universe, light waves from a distant celestial object are stretched, causing their wavelength to become longer. This means the light we receive in a specific waveband was actually emitted by the object at a shorter, bluer wavelength in its rest frame. To accurately calculate the intrinsic flux of a celestial object, it is essential to apply a K-correction based on its z . This demonstrates the tight correlation between z and observed flux (J. B. Oke & A. Sandage 1968).

Building upon the understanding of the relationship between z and observed flux, and to investigate the intrinsic physical differences between BZBs and BZQs, we conducted an in-depth analysis of the differences in their z distributions from the 4LAC-DR3 catalog (M. Ajello et al. 2022b), utilizing the technical procedure outlined in Content 4 of Figure 17. Our statistical analysis of the z distributions for BZBs and BZQs reveals a significant difference between these two populations. The histogram in Figure 10 clearly illustrates the differences in the central tendencies and overall spreads of the two z distributions.

The quantitative metrics in Table 5 show that the mean (0.42) and median (0.31) z of the BZB sample are substantially lower than those of the BZQ sample (mean = 1.19, median = 1.11). This indicates that BZQ objects are, on average, located at greater cosmological distances. As indicated in Table 5, the BZB sample displays a lower mean (0.42) and median (0.31) z compared to the BZQ sample (mean = 1.19, median = 1.11), suggesting that BZQ objects are, on average, located at greater cosmological distances. The BZQ sample covers a broader z range (0.03 – 4.31) than the BZB sample (0 – 3.53), indicating that BZQs include more distant, high- z objects. The BZB sample’s z distribution is sharply peaked at low z and has a long tail, as evidenced by its high skewness (2.68) and kurtosis (10.66). In contrast, the distribution of BZQs is flatter, with a skewness of 0.81 and a kurtosis of 0.86, making it closer to a symmetrical, low-kurtosis distribution. Moreover, a JSD of 0.479 further confirms a fundamental difference between the z distributions of the two samples.

In conclusion, the histogram, statistical metrics, and JSD value all clearly indicate that the redshift distributions of the BZB and BZQ samples are significantly different. Given the tight correlation between redshift and observed flux shown in Equation (6), this disparity in redshift is likely a key factor driving the observed differences in the flux distributions of these two populations.

¹⁰ <http://hyperphysics.phy-astr.gsu.edu/hbase/vision/isql.html>

3.2. Evaluating the Rationality and Merits of Statistical Modeling

The SND, due to its symmetry, desirable mathematical properties, and strong theoretical grounding in the central limit theorem, offers fundamental advantages in statistical modeling. It is widely used to describe natural phenomena and to facilitate statistical inference (A. DasGupta 2008; Z. Cheng 2008). However, in practical applications, especially when dealing with flux data from astronomical observations, the ideal assumption of an SND is often difficult to fulfill. Specifically, observed fluxes in astrophysics are typically constrained by both physical mechanisms and instrumental limitations, such as the non-negativity of flux, and the sensitivity threshold of detectors, resulting in intrinsic truncation at both lower and upper limits. The domain of the independent variable in an SND spans the entire range of real numbers, and its PDF remains nonzero across both positive and negative infinitesimals (J. A. Rice & J. A. Rice 2007). Consequently, directly applying the SND to model data with inherent lower and upper bounds, such as non-negative flux, inevitably assigns nonzero probabilities to physically invalid negative values. This not only violates the physical constraints of the variable but also undermines the normalization integrity of the probability model. In contrast, the TND sets zero probability density outside the domain of the variable and renormalizes the density function within the valid interval. This approach preserves the favorable mathematical properties of the SND while strictly adhering to the physical boundaries of the variable. Therefore, the TND model is well-suited for modeling flux data in astronomical observations, where non-negativity and bounded-domain constraints are inherently present.

In this study, we applied the LOF method (M. M. Breunig et al. 2000) to identify and remove outliers from the raw samples that failed the KS test. By assessing variations in local density, the LOF method sensitively detects locally anomalous data points. To optimize the performance of the LOF method, we systematically investigate various parameter combinations, including the **n_neighbors** and **contamination**, to determine the optimal configuration that minimizes the contamination proportion while satisfying the KS test. This approach ensures effective outlier removal while preserving the overall distribution characteristics of the original dataset to the greatest extent possible.

To quantify the statistical confidence of each source within the fitted flux distribution, we computed the 68.27% (1σ) and 95.45% (2σ) CIs based on the TND. Instead of conventional symmetric interval definitions, we adopted a CDF-based approach, which is appropriate for distributions exhibiting asymmetry due to truncation (R. J. Hyndman & Y. Fan 1996; C. Ialongo 2019). Specifically, the 1σ interval spans the 15.87% to 84.14% quantiles, and the 2σ interval spans from the 2.28% to 97.73% quantiles. This method does not rely on the assumption of symmetry around the mean and more accurately reflects the true probability distribution within the truncated domain. Samples that fall within the 2σ CI are generally regarded as statistically consistent with the overall population, whereas those outside this range are likely to exhibit distinct physical properties.

The z-score offers a quantitative measure of how far a given sample deviates from the population mean. A larger absolute z-score indicates more extreme radiative behavior relative to the overall population, reflecting a greater departure from the distribution's central tendency. Conversely, a z-score near zero suggests that the sample lies close to the population mean and is more representative of the overall distribution. By integrating z-score analysis with CIs, this study offers a precise characterization of each sample's relative position and degree of deviation within the distribution. The magnitude of this deviation is particularly important for identifying potential outliers or candidate sources (P. J. Rousseeuw & M. Hubert 2011; S. A. Shaikh & H. Kitagawa 2014; S. Roy & T. Suyama 2024).

In practical applications, to assess whether the multi-wavelength flux characteristics of a given blazar candidate are statistically consistent with the flux distribution models derived from a large sample, this study determines the candidate's relative position within the flux distribution of each band and computes its corresponding z-score. For a specific band, the combined use of the z-score and CIs intuitively reflects the position of the target source within the overall distribution, thereby enabling an assessment of whether its flux characteristics are consistent with those of the overall sample. If the z-score of the target source falls within the 2σ CI, it is considered statistically consistent with the flux distribution of the large sample. Furthermore, achieving statistical consistency across multiple wavebands provides additional support for the common-source hypothesis in cross-identification analyses. The method of Content 4 of Figure 17 offers effective visualization, presenting the analytical results in a clear and intuitive manner that enhances statistical interpretability. Moreover, as shown in Table 11, except for the 74 MHz band where a few outliers were excluded, the flux samples in all other bands passed the KS test, thereby validating the robustness and generalizability of the proposed modeling framework. This framework enables rapid screening and batch processing of multi-source flux data under a unified standard, substantially improving the efficiency of large-sample statistical analyses.

3.3. Identification of 17 New GeV Blazar Candidates

First, we used **Fermipy** to construct the DR2 with positional uncertainties. Following Content 1 in Figure 12, we then built the 5BZCAT_err, also incorporating positional uncertainties. Subsequently, we performed spatial cross-identification according to Content 2 in Figure 14, successfully identifying 17 new GeV blazar candidates. To further evaluate their correlation from a physical perspective, we extracted multi-wavelength flux data for the 5BZCAT_err sources according to Content 3 of Figure 17. Subsequently, following Content 4 of the same pipeline, we conducted a comparative analysis to assess whether the flux distributions of BZBs and BZQs differ across various wavebands. The results reveal significant differences in the 1.4 GHz and 0.1–2.4 keV bands, whereas the differences in other bands are relatively minor. Building on this, we performed statistical modeling of the logarithmic flux distributions for each band. We propose the following hypothesis: a source can be considered statistically consistent with a given class in terms of its multi-wavelength radiative behavior if its z-scores across multiple bands all fall within the 2σ CIs of the corresponding distributions for that class. Conversely, a substantial deviation in any waveband likely indicates differences in the physical processes associated with emission, such as the radiation mechanism, jet formation, or Doppler beaming effects.

Based on the established distribution models and the corresponding transformation parameters detailed in Table 11, we applied the Box–Cox transformation to the flux data of the 17 selected blazars. The transformed values were then mapped onto the TND models for their respective source classes, and their relative positions within the population distributions were assessed using z-scores and CIs. The mapping results are summarized in Table 4. Specifically, the multi-band flux z-scores for 9 BZBs and 6 BZQs are near zero and fall entirely within the 2σ CIs, indicating that their fluxes in the corresponding bands are close to the population mean and lie within the statistically “normal” range. As discussed in Section 3.2, this statistical consistency suggests that these sources likely share similar physical mechanisms for their multi-wavelength radiative behavior, thereby providing further support for the common-source hypothesis.

Notably, the fluxes of two sources—5BZQ J1215+3448 (z-score = -2.417) and 5BZQ J1243+4043 (z-score = -3.102)—in the 0.1–100 GeV band exhibit significant deviations from the distribution model, as shown in Figure 11. These fluxes are significantly below the mean of the overall population, with z-scores falling outside the 2σ CI, indicating a relatively weak activity state. The Box–Cox transformed flux of 5BZQ J1243+4043 falls slightly below the lower bound of the TND model. Although the flux of 5BZQ J1215+3448 remains within the truncated range, it still exhibits a significant deviation from the mean of the overall population. Further analysis reveals that, in the energy range above 100 MeV, the TS values for 5BZQ J1243+4043 and 5BZQ J1215+3448 in DR2 are 17.45 and 20.33, respectively, indicating that both sources exhibit very weak γ -ray signals given the current level of data accumulation. As shown in Table 1, by comparing the energy flux (Energy_Flux100) between 100 MeV and 1 TeV in 4FGL-DR3 and 4FGL-DR4, we observed an increasing phenomenon in the Energy_Flux100 of certain sources as observational data accumulated. Specifically, a total of 3,578 sources have a Ratio_Eflux greater than 1, where Ratio_Eflux is defined as the ratio of Energy_Flux100_v35 to Energy_Flux100_v31. This result indicates that the Energy_Flux100 of these sources in 4FGL-DR4 exhibits varying degrees of increase compared to their corresponding values in 4FGL-DR3, including 1,056 blazars. The investigation results indicate that many blazar candidates, which exhibited low fluxes in earlier catalog versions, showed increases in flux as subsequent observational data accumulated. Therefore, we speculate that the currently low flux values of 5BZQ J1243+4043 and 5BZQ J1215+3448 may merely reflect their observed states during the initial phases of data accumulation.

Additionally, the z-score values of 5BZQ J1243+4043 at 1.4 GHz and 5 GHz are close to the means of the corresponding distributions and lie within the 1σ CIs. For 5BZQ J1215+3448, the z-scores across the 74 MHz to 2.4 keV bands fall within the 2σ CIs. These results indicate that, in the radio or X-ray bands, the characteristics of flux distributions of these two sources exhibit no systematic deviation from the statistical model. Besides, given that the TS values of 5BZQ J1243+4043 and 5BZQ J1215+3448 are near the Fermi-LAT detection threshold and display distinct source features in their TS maps, we anticipate that these two sources will likely gradually approach the high-confidence region of the corresponding distribution model as observational data continue to accumulate. Therefore, we retain these sources in the sample and designate them as GeV BZQ candidates positioned near the boundary of the distribution model. We recommend the continued monitoring and validation of the evolution of their γ -ray flux within the context of our distribution model.

Through this analysis, we modeled the multi-band flux distributions of 17 GeV blazars and found that 9 BZBs and 6 out of 8 BZQs exhibit distributional characteristics consistent with those of the larger sample, showing only minor

deviations from the population mean. Considering the strong spatial association between these 15 γ -ray sources and the blazar objects in the 5BZCAT_err, we suggest that they likely constitute a high-probability associated population. In particular, 5BZQ J1215+3448 and 5BZQ J1243+4043 exhibit flux distribution characteristics in the radio and/or X-ray bands that closely align with those of the larger population, along with strong spatial associations and significant GeV signals. Consequently, we propose them as promising candidates for GeV BZQs. Due to limited photon counts, the low flux levels in the 0.1–100 GeV band for these two sources necessitate ongoing observations to confirm the similarity of their GeV flux distribution characteristics.

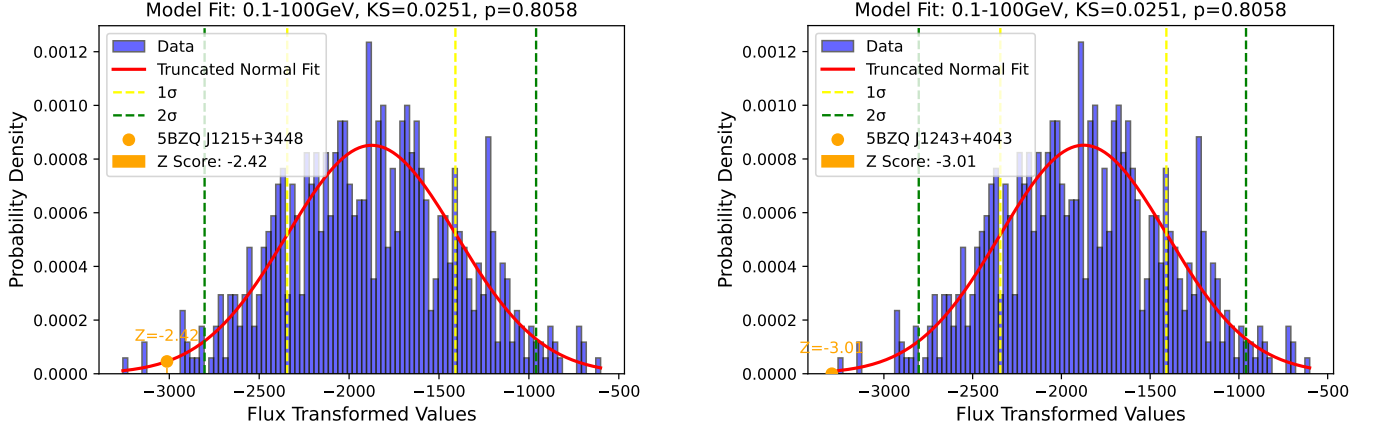


Figure 11. Analysis results of the TND model for 5BZQ J1215+3448 and 5BZQ J1243+4043 in the 0.1–100 GeV band. Similar details are illustrated in Figure 5.

4. CONCLUSIONS

The classification of blazars and their physical origin is one of the core questions in high-energy astrophysics. To delve deeper into the intrinsic differences between BZBs and BZQs, this study constructs a full-process analysis Pipeline that covers data collection, new source identification, statistical modeling, and tracing of physical origins. This Pipeline not only systematically quantifies the significant differences in observational and physical properties between BZBs and BZQs, providing robust multi-dimensional evidence for the classic *blazar dichotomy*, but also offers strong statistical support for the classification of new or ambiguously classified blazar candidates. The main findings and conclusions of this study are as follows:

1. Based on 16 years of Fermi-LAT observation data, this study re-analyzed the sources in the early DR1 gamma-ray source catalog using the **Fermipy** toolkit to address its lack of crucial elliptical positional errors. Ultimately, we released a new, more complete catalog, DR2, featuring precise elliptical errors and other comprehensive parameters.
2. To address the lack of crucial positional errors in the 5BZCAT blazar catalog, we integrated it with the NED database, systematically populated the positional uncertainties for all 3,561 sources, and constructed a new catalog, 5BZCAT_err, suitable for probabilistic cross-matching.
3. By cross-matching the DR2 with 5BZCAT_err, we identified 17 high-confidence GeV blazars. These matches have high association probabilities, and their association has been independently verified using **TOPCAT** and **DS9**.
4. A systematic analysis of the 17 new GeV blazars was conducted using **Fermipy**. The results show no significant spatial extension or spectral curvature for any of the sources. In terms of variability, most sources were not significantly variable, except for J1043.7+5323, which exhibited strong variability confirmed across multiple timescales.
5. To systematically compare the flux distributions of BZBs and BZQs, we collected multi-wavelength flux data for sources in the 5BZCAT_err. We then quantified their differences using two methods: the MAD for eight

statistical indicators, and the JSD for the overall probability distributions. Both analytical methods consistently show systematic differences between BZBs and BZQs across all observed bands. Specifically, the MAD analysis identifies kurtosis as the most discriminative statistical metric, and the JSD analysis highlights the 1.4 GHz and 0.1–2.4 keV bands as those with the largest overall distributional differences.

6. To address the limitations of single-band metrics for blazar classification (e.g., small sample sizes and incomplete information), we introduce a new model combining the Box-Cox transformation and truncated normal distribution (TND) fitting, termed the “Box-Cox + TND” model. The model proves to be robust and widely applicable, successfully fitting nearly all BZB and BZQ flux distributions.
7. This study, for the first time, applies the “Box-Cox + TND” model to assess the statistical consistency between the multi-band flux distributions of the 17 newly discovered blazars and the large 5BZCAT sample. The results reveal that the flux values for the vast majority of these new sources are within the 1σ or 2σ confidence intervals of the model distribution for their respective samples. This finding suggests a high degree of statistical agreement with the known blazar population, offering strong evidence for their accurate classification and common-source hypothesis.
8. This study, for the first time, utilizes the JSD to quantify the distributional differences between BZBs and BZQs in four key physical properties: synchrotron peak frequency, jet power, Doppler beaming factor, and redshift. We found that the distributions of these four properties are significantly different for the two classes of objects, with all corresponding JSD values exceeding 0.3. This finding offers robust, multi-dimensional statistical support for the traditional optically-based blazar dichotomy.

Table 6. Explanation of Keywords

Column	Unit	Description
Table 1		
Source_Name	...	Name of the source in 4FGL-DR3 and 4FGL-DR4
RAJ2000	deg	Right ascension
DEJ2000	deg	Declination
Signif_Avg_v31	σ	Source significance in σ units over the 100 MeV to 1 TeV band in 4FGL-DR3
Signif_Avg_v35	σ	Source significance in σ units over the 100 MeV to 1 TeV band in 4FGL-DR4
Ratio_Sig	...	Ratio of Signif_Avg_v35 to Signif_Avg_v31
Energy_Flux100_v31	$\text{erg cm}^{-2} \text{ s}^{-1}$	Energy flux from 100 MeV to 100 GeV obtained by spectral fitting
Energy_Flux100_v35	$\text{erg cm}^{-2} \text{ s}^{-1}$	Energy flux from 100 MeV to 100 GeV obtained by spectral fitting
Ratio_Eflux	...	Ratio of Energy_Flux100_v35 to Energy_Flux100_v31
Table 7		
5BZ_Name	...	Source name from 5BZCAT
NED_Name	...	Matched object name from NED
RA	deg	Right ascension
DEC	deg	Declination
RA_m	deg	Right ascension of the matched NED candidate
DEC_m	deg	Declination of the matched NED candidate
Sep	arcmin	Angular separation between the source and the candidate
Conf95_Maj	arcsec	Semi-major axis of the 95% confidence positional error uncertainty ellipse
Conf95_Min	arcsec	Semi-minor axis of the 95% confidence positional error ellipse
Unc_PA	deg	Position angle of the uncertainty ellipse
Refcode	...	Reference code for the matched NED source
In_Ellipse	...	Within NED ellipse? (TRUE/FALSE)

Column	Unit	Description
Table 8		
Name	...	Source name from 5BZCAT_err
RA	deg	Right Ascension
DEC	deg	Declination
Conf95_Maj	arcsec	Semi-major axis of the 95% confidence positional error ellipse
Conf95_Min	arcsec	Semi-minor axis of the 95% confidence positional error ellipse
Unc_PA	deg	Position angle of the uncertainty ellipse
Refcode	...	Reference code for the matched NED source
Opt_Mag	...	Apparent optical magnitude
Table 2		
5BZ_Name	...	Source name from 5BZCAT_err
DR2_Name	...	Source name in DR2
DR2_RA	deg	Right ascension
DR2_DEC	deg	Declination
5BZ_Name	...	Matched source name from the 5BZCAT_err
5BZ_RA	deg	Right ascension of the matched 5BZCAT_err counterpart
5BZ_DEC	deg	Declination of the matched 5BZCAT_err counterpart
Sep	arcsec	Angular separation between the source positions in DR2 and 5BZCAT_err
Psingle	...	Single-match probability
Pany	...	Any-match probability
Pi	...	Individual relative match probability
Table 3		
Name_5BZCAT	...	Source name from 5BZCAT
Name_DR2	...	Source name in DR2
TS _{cur,lp}	...	Curvature TS value for the LogParabola spectral model
TS _{cur,plec}	...	Curvature TS value for PowerLaw with exponential cutoff model
TS _{ext,disk}	...	Extension TS value for Disk model
TS _{ext,gauss}	...	Extension TS value for 2D-Gaussian model
TS _{var}	...	Variability index
Table 9		
Type	...	Source class
Min	...	Minimum value of log10(flux) distribution
Max	...	Maximum value of log10(flux) distribution
Mean	...	Mean of log10(flux) distribution
Median	...	Median of log10(flux) distribution
Mode	...	Mode of log10(flux) distribution
Std	...	Standard deviation
Skewness	...	Measure of skewness
Kurtosis	...	Measure of kurtosis
JSD(BZB & BZQ)	...	Jensen–Shannon distance between the flux distributions of BZBs and BZQs
Table 10		
Name	...	Source name
74 MHz	Jy	Flux density at 74 MHz
Uncertainty	Jy	Flux uncertainty at 74 MHz
Refcode	...	Reference for the 74 MHz flux
Table 11		
Waveband	...	Observational waveband

Column	Unit	Description
Type	...	Source class
λ	...	Box–Cox transformation factor
Mean	...	Mean of the Box–Cox transformed fluxes
Std	...	Standard deviation of the Box–Cox transformed fluxes
KS	...	KS statistic
p	...	P-value corresponding to the KS statistic
TruncNorm	...	Boolean flag indicating if the TND model fit is valid

Table 4

Name	...	Name of the source
Waveband	...	Observational frequency band
Type	...	Source class
Box–Cox Flux	...	Box–Cox transformed flux value
CI	...	The range where the target object lies within the confidence interval
Z-score	...	Z-score of the TND

Table 5

Min	...	Minimum of the distribution
Max	...	Maximum of the distribution
Mean	...	Mean of the distribution
Median	...	Median of the distribution
Mode	...	Mode of the distribution
Std	...	Standard deviation
Skewness	...	Skewness of the distribution
Kurtosis	...	Kurtosis of the distribution
JSD	...	Jensen–Shannon distance

Keywords of 4FGL-Xiang-DR2.fit

Name	...	Source name in 4FGL-Xiang-DR2
RAJ2000	deg	Right ascension (J2000)
DEJ2000	deg	Declination (J2000)
Conf_68_SemiMajor	arcsec	Semi-major axis of the 68% positional uncertainty ellipse
Conf_68_SemiMinor	arcsec	Semi-minor axis of the 68% positional uncertainty ellipse
Conf_95_SemiMajor	arcsec	Semi-major axis of the 95% confidence region
Conf_95_SemiMinor	arcsec	Semi-minor axis of the 95% confidence region
Pos_angle	deg	Position angle of the error ellipse
SpatialType	...	Spatial model
SpectrumType	...	Spectral model
Spectral_Index	...	Spectral index of the Powerlaw model
Index_err	...	1σ Uncertainty of the spectral index
TS	...	TS value for source detection significance
Npred	...	Predicted photon counts
Flux100	$\text{ph cm}^{-2} \text{s}^{-1}$	Photon flux in 100 MeV to 1 TeV energy band
Flux1000	$\text{ph cm}^{-2} \text{s}^{-1}$	Photon flux in 1 GeV to 1 TeV energy band
Flux10000	$\text{ph cm}^{-2} \text{s}^{-1}$	Photon flux in 10 GeV to 1 TeV energy band
Flux100_err	$\text{ph cm}^{-2} \text{s}^{-1}$	1σ uncertainty of Flux100
Flux1000_err	$\text{ph cm}^{-2} \text{s}^{-1}$	1σ uncertainty of Flux1000
Flux10000_err	$\text{ph cm}^{-2} \text{s}^{-1}$	1σ uncertainty of Flux10000
Eflux100	$\text{erg cm}^{-2} \text{s}^{-1}$	Energy flux in 100 MeV to 1 TeV band
Eflux1000	$\text{erg cm}^{-2} \text{s}^{-1}$	Energy flux in 1 GeV to 1 TeV band
Eflux10000	$\text{erg cm}^{-2} \text{s}^{-1}$	Energy flux in 10 GeV to 1 TeV band
Eflux100_err	$\text{erg cm}^{-2} \text{s}^{-1}$	1σ uncertainty of Eflux100

Column	Unit	Description
Eflux1000_err	$\text{erg cm}^{-2} \text{s}^{-1}$	1σ uncertainty of Eflux1000
Eflux10000_err	$\text{erg cm}^{-2} \text{s}^{-1}$	1σ uncertainty of Eflux10000
Keywords of 5BZCAT_multi-band_flux.xlsx		
Name	...	Source name from 5BZCAT
74MHz	Jy	Flux density at 74 MHz
74MHz_Uncertainty	Jy	Uncertainty of 74 MHz flux
74MHz_Refcode	...	Reference code for 74 MHz flux
365MHz	Jy	Flux density at 365 MHz
365MHz_Uncertainty	Jy	Uncertainty of 365 MHz flux
365MHz_Refcode	...	Reference code for 365 MHz flux
843MHz	Jy	Flux density at 843 MHz
843MHz_Uncertainty	Jy	Uncertainty of 843 MHz flux
843MHz_Refcode	...	Reference code for 843 MHz flux
1.4GHz	Jy	Flux density at 1.4 GHz
1.4GHz_Uncertainty	Jy	Uncertainty of 1.4 GHz flux
1.4GHz_Refcode	...	Reference code for 1.4 GHz flux
4.85GHz	Jy	Flux density at 4.85 GHz
4.85GHz_Uncertainty	Jy	Uncertainty of 4.85 GHz flux
4.85GHz_Refcode	...	Reference code for 4.85 GHz flux
20GHz	Jy	Flux density at 20 GHz
20GHz_Uncertainty	Jy	Uncertainty of 20 GHz flux
20GHz_Refcode	...	Reference code for 20 GHz flux
0.1-2.4keV	$\text{erg cm}^{-2} \text{s}^{-1}$	X-ray flux in 0.1–2.4 keV band
0.1-2.4keV_Uncertainty	$\text{erg cm}^{-2} \text{s}^{-1}$	Uncertainty of 0.1–2.4 keV flux
0.1-2.4keV_Refcode	...	Reference code for 0.1–2.4 keV flux
0.3-10keV	$\text{erg cm}^{-2} \text{s}^{-1}$	X-ray flux in 0.3–10 keV band
0.3-10keV_Uncertainty	$\text{erg cm}^{-2} \text{s}^{-1}$	Uncertainty of 0.3–10 keV flux
0.3-10keV_Refcode	...	Reference code for 0.3–10 keV flux
0.1-100GeV	$\text{erg cm}^{-2} \text{s}^{-1}$	Gamma-ray flux in 0.1–100 GeV band
0.1-100GeV_Uncertainty	$\text{erg cm}^{-2} \text{s}^{-1}$	Uncertainty of 0.1–100 GeV flux
0.1-100GeV_Refcode	...	Reference code for 0.1–100 GeV flux

5. DATA AVAILABILITY

All data products generated in this study have been publicly released through the [China-VO PaperData repository](#). The released datasets include:

1. Refined γ -ray source catalog, `4FGL-Xiang-DR2.fit`; described in Section 2.1.
2. Comparison of Signif_Avg and Energy_Flux100 between 4FGL-DR3 and 4FGL-DR4, `Comparison_v31_v35.xlsx`; described in Section 3.1.
3. Elliptical positional uncertainties and optical magnitudes for 5BZCAT sources, `5BZCAT_err.fit`; described in Section 2.3.
4. Manually verified cross-matching results and spatial association plots for 62 sources lacking positional uncertainties, `62Figures.tar.xz`; described in Section 2.3.
5. GeV emission characteristic analysis for 17 new candidate blazars, including:
 - `TScmap17.tar.xz`; described in Appendix B.
 - `SED17.tar.xz`; described in Section 2.5.2.

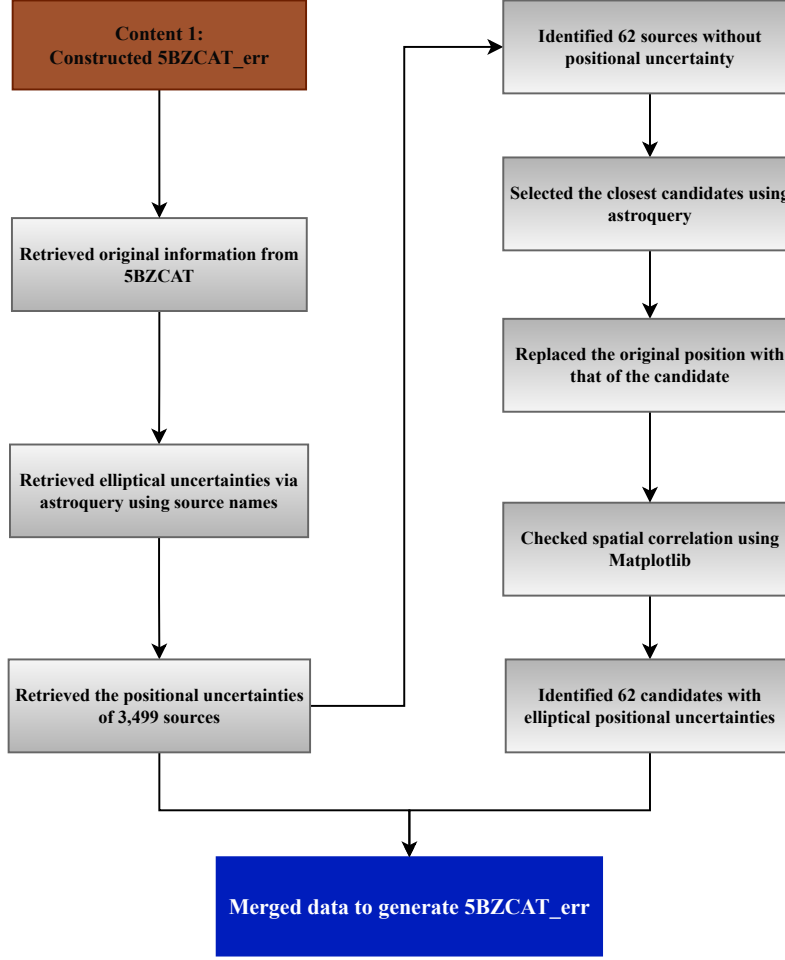


Figure 12. Workflow for constructing 5BZCAT_err.

- LC17.tar.xz; described in Section 2.5.3.

6. Standardized multi-wavelength flux data for 3,442 blazars, 5BZCAT_multi-band_flux.xlsx; described in Section C.1.
7. The fitting plots of the TND model after Box-Cox transformation for 17 blazar candidates, Model_fitting_results.tar.xz; described in Section 2.6.3

Detailed descriptions of each dataset and usage instructions are provided in the accompanying Readme.txt.

APPENDIX

A. THE 5BZCAT_ERR CONSTRUCTION PIPELINE

Given that the 5BZCAT data had been uploaded to NED (E. Massaro et al. 2015), we initially attempted to manually extract the positional uncertainties for each source from the NED website (NASA/IPAC Extragalactic Database 2019). However, due to the large sample size, manual extraction proved to be inefficient and time-consuming. To efficiently compile a version of the 5BZCAT with complete positional uncertainty information, we developed a targeted analytical pipeline, which is illustrated in Figure 12. The corresponding construction procedure is detailed below:

Step 1: We retrieved the complete parameter dataset for 3,561 sources from the official 5BZCAT website. Using the source names and their alternative designations as input, we extracted the positional uncertainties from the NED

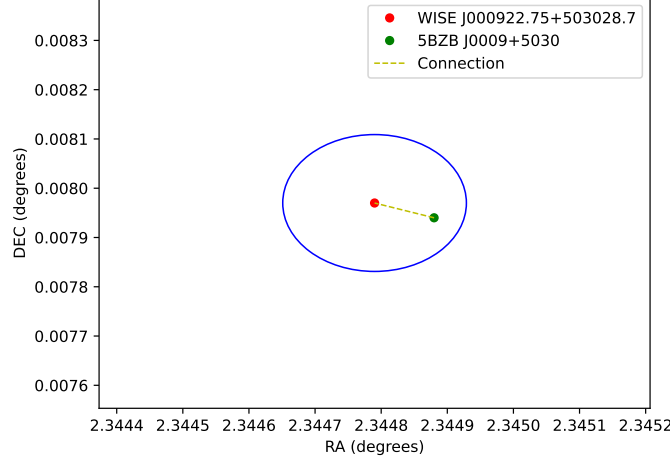


Figure 13. Spatial association between the 5BZCAT source (green) and the NED candidate (red), exemplified by WISE J000922.75+503028.7 and 5BZB J0009+5030. The blue ellipse represents the positional uncertainty of the NED candidate, while the dashed yellow line indicates the angular separation between the two sources.

via the `ned.get_table()` function¹¹ of the Python package `astroquery` (A. Ginsburg et al. 2019). In this step, we successfully obtained positional uncertainties for 3,499 sources.

Step 2: In Step 1, we identified that positional uncertainty information was missing for 62 sources. To address this, we utilized the target positions provided by 5BZCAT as input and employed the `ned.query_region()` function to retrieve relevant positional data. To identify potential matching candidates, we adopted the minimum angular separation as the filtering criterion. We compiled the association results between NED and 5BZCAT into Table 7. Subsequently, we utilized the `matplotlib.patches.Ellipse()` method (J. D. Hunter 2007) to generate spatial relationship plots between the target sources and their candidates. Upon examining the associations for the 62 objects, we confirmed that the candidates are spatially correlated with the target sources. For example, the spatial relationship between 5BZB J0009+5030 and WISE J000922.75+503028.7, as shown in Figure 13, indicates a high degree of positional coincidence. The association result figures for the 62 objects are packaged in `62Figures.tar.xz`, as referenced in Section 5. The NED-derived candidate positions were subsequently adopted as the positional data for these 62 objects in the following analyses.

Step 3: We compiled and recorded the positional uncertainty information of 3,561 objects into a new catalog, named `5BZCAT_err`. This catalog also incorporates the optical band magnitude data provided by 5BZCAT. Its basic format is shown in Table 8, and the complete FITS version is available in Section 5.

B. THE CROSS-IDENTIFICATION PIPELINE

We designed a cross-identification pipeline, as illustrated in Figure 14. Following this pipeline, we conducted a spatial probability analysis based on the official `nway` tutorial. Specifically, DR2 was used as the primary catalog and `5BZCAT_err` as the matching catalog. To improve the matching accuracy, we adopted an elliptical error model that incorporates the semi-major axis, semi-minor axis, and position angle. Furthermore, to improve the precision of posterior probability estimates in the cross-matching process, we incorporated the optical magnitude information (from the `Opt_Mag` column of `5BZCAT_err`) as a prior distribution. To identify high-probability matches, all results were filtered using stringent probabilistic thresholds, requiring the any-match probability (p_{any}) and the individual relative match probability (p_i) to each exceed 85%. The definitions of these two probabilities are detailed below:

- P_{any} : The probability that a given source in the primary catalog has at least one counterpart in the secondary catalog.
- P_i : The probability that a candidate is the true counterpart of the target source, based on its positional match and incorporating other prior information.

¹¹ <https://astroquery.readthedocs.io/en/latest/ipac/ned/ned.html>

Table 7. Spatial Association Between 5BZCAT Source and NED Candidate

5BZ_Name	NED_Name	RA	DEC	RA_m	DEC_m	Sep	Conf95_Maj	Conf95_Min	Unc_PA	Refcode	In_Ellipse
5BZG J0001-1031	WISEA J000157.26-103117.4	0.489	-10.521	0.489	-10.522	0.003	0.22875	0.19675	0	2013wise.rept....1C	TRUE
5BZQ J0006-4245	[HB89] 0003-430	1.582	-42.755	1.582	-42.755	0.001	0.21325	0.213	0	2013wise.rept....1C	TRUE
5BZB J0047+5657	WISEA J004700.43+565742.4	11.752	56.962	11.752	56.962	0	0.00025	0.0002	0	2019ApJS...242....5X	TRUE
5BZB J0116-6153	WISEA J011619.62-615343.4	19.082	-61.895	19.082	-61.895	0.001	0.10925	0.10825	90	2013wise.rept....1C	TRUE
5BZB J0133-4414	WISEA J013306.37-441421.4	23.277	-44.239	23.277	-44.239	0.001	0.10325	0.10225	90	2013wise.rept....1C	TRUE
5BZG J0320-7500	WISEA J032052.20-750038.1	50.218	-75.011	50.218	-75.011	0	0.0975	0.09175	0	2013wise.rept....1C	TRUE
5BZU J0416-4355	SUMSS J041605-435516	64.024	-43.921	64.024	-43.921	0.002	0.5	0.5	0	2013ApJS...206....13M	TRUE
5BZB J0425-5331	WISEA J042504.27-533158.2	66.268	-53.533	66.268	-53.533	0	0.083	0.08125	90	2013wise.rept....1C	TRUE
5BZB J0433-4502	APMUKS(BJ) B043142.34-450909.3	68.308	-45.049	68.308	-45.049	0	0.5	0.5	0	2011MNRAS.417.2651M	TRUE
5BZB J0434-2342	WISEA J043428.98-234205.3	68.621	-23.701	68.621	-23.702	0.002	0.15	0.15	0	2007ApJS...171....61H	TRUE
5BZU J0532-0307	WISEA J053207.51-030707.5	83.031	-3.119	83.031	-3.119	0	0.15	0.15	0	2007ApJS...171....61H	TRUE
5BZB J0556-4351	WISEA J055618.74-435146.0	89.078	-43.863	89.078	-43.863	0.001	0.10375	0.0995	90	2013wise.rept....1C	TRUE
5BZU J0737+3216	WISEA J073705.58+321632.1	114.273	32.276	114.273	32.276	0.003	0.4065	0.37625	0	2013wise.rept....1C	TRUE
5BZG J0748+2115	SPIDERS 2_11411	117.181	21.263	117.181	21.263	0.001	5	5	0	2015ApJ...807..178W	TRUE
5BZB J0751+3928	WISEA J075144.93+392817.5	117.937	39.472	117.937	39.472	0.001	0.306	0.2865	0	2013wise.rept....1C	TRUE
5BZG J0835+1517	WISEA J083548.14+151717.0	128.951	15.288	128.951	15.288	0.001	0.1145	0.11375	90	2013wise.rept....1C	TRUE
5BZG J0906+4636	B3 0902+468	136.565	46.605	136.565	46.605	0	0.00025	0.00025	0	2021AJ....162..121H	TRUE
5BZG J0950+1804	WISEA J095000.30+180418.7	147.501	18.072	147.501	18.072	0.002	0.139	0.134	0	2013wise.rept....1C	TRUE
5BZU J1010-0730	PKS 1007-07	152.521	-7.506	152.521	-7.506	0.001	0.18225	0.17225	0	2013wise.rept....1C	TRUE
5BZU J1059+4051	FIRST J105951.9+405113	164.966	40.854	164.966	40.854	0.004	0.342	0.319	172	1995ApJ...450..559B	TRUE
5BZB J1110-1835	WISEA J111027.77-183552.7	167.616	-18.598	167.616	-18.598	0.001	0.1365	0.13175	0	2013wise.rept....1C	TRUE
5BZB J1242-1653	GALEXASC J124220.51-165303.8	190.585	-16.884	190.585	-16.884	0	0.5	0.5	0	2011MNRAS.417.2651M	TRUE
5BZG J1243+5212	WISEA J124308.98+521245.0	190.787	52.213	190.787	52.213	0.001	0.13275	0.12925	0	2013wise.rept....1C	TRUE
5BZG J1301+4634	WHL J130132.6+463403	195.386	46.567	195.386	46.567	0	5	5	0	2015ApJ...807..178W	TRUE
5BZU J1431-0052	WISE J143112.91-005244.4	217.805	-0.877	217.805	-0.877	0.002	0.28	0.28	0	2023arXiv.230606308D	TRUE
5BZG J1451+5800	SDSS J145111.70+580003.0	222.799	58.001	222.799	58.001	0.002	0.5	0.5	0	2016SDSSD.C....0000:	TRUE
5BZG J1539+4143	SDSS J153951.38+414325.4	234.964	41.724	234.964	41.724	0.002	0.5	0.5	0	2007SDSS6.C....0000:	TRUE
5BZG J1548+6310	WISEA J154828.42+631051.1	237.118	63.181	237.118	63.181	0	0.1175	0.114	0	2013wise.rept....1C	TRUE
5BZG J1624+3726	SDSS J162443.36+372642.4	246.181	37.445	246.181	37.445	0.001	0.5	0.5	0	2016SDSSD.C....0000:	TRUE
5BZQ J1717-5155	WISEA J171734.65-515532.0	259.394	-51.926	259.394	-51.926	0.001	0.21075	0.20675	0	2013wise.rept....1C	TRUE
5BZB J1830+1324	WISEA J183000.76+132414.3	277.503	13.404	277.503	13.404	0.001	0.10925	0.1055	90	2013wise.rept....1C	TRUE
5BZB J1844+5709	RBPL J1844+5709	281.212	57.161	281.212	57.161	0	0.5	0.5	0	2014ApJS...215....14D	TRUE
5BZB J1849+2748	WISEA J184931.74+274800.8	282.382	27.800	282.382	27.800	0.001	0.09425	0.09325	90	2013wise.rept....1C	TRUE
5BZB J1925-2219	WISEA J192539.77-221935.1	291.416	-22.326	291.416	-22.326	0	0.000275	0.00025	90	2019ApJS...242....5X	TRUE
5BZB J2036+6553	WISE J203620.13+655314.5	309.084	65.887	309.084	65.887	0	0.5	0.5	0	2014ApJS...215....14D	TRUE
5BZU J2208+6519	WISEA J220803.09+651938.9	332.013	65.327	332.013	65.327	0	0.00025	0.00025	0	2021AJ....162..121H	TRUE
5BZU J2250-4206	WISEA J225022.22-420613.4	342.593	-42.104	342.593	-42.104	0.001	0.0955	0.0925	90	2013wise.rept....1C	TRUE
5BZB J0105+3928	4FGL J0105.1+3929	16.289	39.471	16.291	39.496	1.527	274.14	228.06	137	2020ApJS...247....33A	TRUE
5BZB J0110-0415	GALEXASC J011030.92-041531.5	17.629	-4.259	17.629	-4.259	0.012	1.203323	1.203323	0	2012GASC.C....0000S	TRUE
5BZB J0144+2705	CRATES J0144+2705 NED02	26.140	27.084	26.140	27.084	0.002	0.15	0.15	0	2007ApJS...171....61H	TRUE
5BZB J0309-3604	GALEXASC J030902.41-360404.3	47.260	-36.068	47.260	-36.068	0.003	0.5	0.5	0	2011MNRAS.417.2651M	TRUE
5BZB J0409-0400	4FGL J0409.8-0359	62.444	-4.001	62.463	-3.987	1.421	223.65	216.99	139	2020ApJS...247....33A	TRUE
5BZB J0702-1951	3FHL J0702.6-1950	105.679	-19.856	105.678	-19.852	0.268	110.97	98.19	130	2020ApJS...247....33A	TRUE
5BZB J1129+3756	3FGL J1129.0+3758	172.264	37.949	172.253	37.972	1.441	162	162	0	2018ApJS...237....32A	TRUE
5BZB J1603-4904	2FGL J1603.8-4904	240.961	-49.068	240.961	-49.068	0.002	15	15	0	2013ApJ...764..135S	TRUE
5BZB J2149+0322	3FHL J2149.8+0322	327.424	3.381	327.441	3.384	1.019	123.48	123.48	0	2018ApJS...237....32A	TRUE
5BZB J2258-3644	3FHL J2258.1-3643	344.561	-36.743	344.562	-36.750	0.43	165.6	165.6	0	2018ApJS...237....32A	TRUE
5BZG J0040-2340	4FGL J0040.4-2340	10.104	-23.667	10.101	-23.670	0.256	306.36	297.99	23	2020ApJS...247....33A	TRUE
5BZG J0106+2539	WHL J010611.0+253930	16.546	25.658	16.546	25.658	0.006	5	5	0	2015ApJ...807..178W	TRUE
5BZG J0946+5819	6C B094238.5+583306	146.560	58.327	146.554	58.321	0.443	63.7	54.3	0	1990MNRAS.246..256H	TRUE
5BZG J1147+3501	WISEA J114722.13+350107.5	176.842	35.019	176.842	35.019	0.002	0.087	0.084	90	2013wise.rept....1C	TRUE
5BZG J1531+0852	RX J1531.5+0851	232.904	8.879	232.899	8.864	0.938	150	150	0	2000ApJS...129..435B	TRUE
5BZG J1755+6236	6C B175524.9+623700	268.952	62.612	268.957	62.611	0.161	24.3	21.6	179	1990MNRAS.246..256H	TRUE
5BZQ J0845-5555	4FGL J0845.7-5556	131.457	-55.924	131.447	-55.949	1.53	198.09	190.35	57	2020ApJS...247....33A	TRUE
5BZU J0023+4456	6C B002051.6+444042	5.898	44.943	5.882	44.955	0.972	91.6	64.4	0	1993MNRAS.263....25H	TRUE
5BZU J0729-1320	CXO J072917.9-132002	112.324	-13.334	112.325	-13.334	0.034	8.78	8.78	0	2010ApJS...189....37E	TRUE
5BZU J0804-1712	CGMW 2-2082	121.140	-17.201	121.150	-17.193	0.756	50	50	0	1991PASJ...43..449S	TRUE
5BZU J1238-1959	3FGL J1238.2-1958	189.602	-19.987	189.565	-19.983	2.088	138.96	138.96	0	2018ApJS...237....32A	TRUE
5BZU J1259-2310	3FHL J1259.0-2311	194.785	-23.177	194.772	-23.183	0.781	107.64	107.64	0	2018ApJS...237....32A	TRUE
5BZU J1448+0402	[WB92] 1446+0410	222.210	4.039	222.216	4.014	1.554	182	182	0	1992ApJS...79..331W	TRUE
5BZU J1911+1611	4FGL J1912.0+1612	287.993	16.196	288.021	16.202	1.641	451.8	435.15	42	2020ApJS...247....33A	TRUE
5BZU J2327+1524	1WGA J2327.3+1525	351.842	15.410	351.847	15.420	0.665	52.6	52.6	0	2000WGA....C....0000W	TRUE

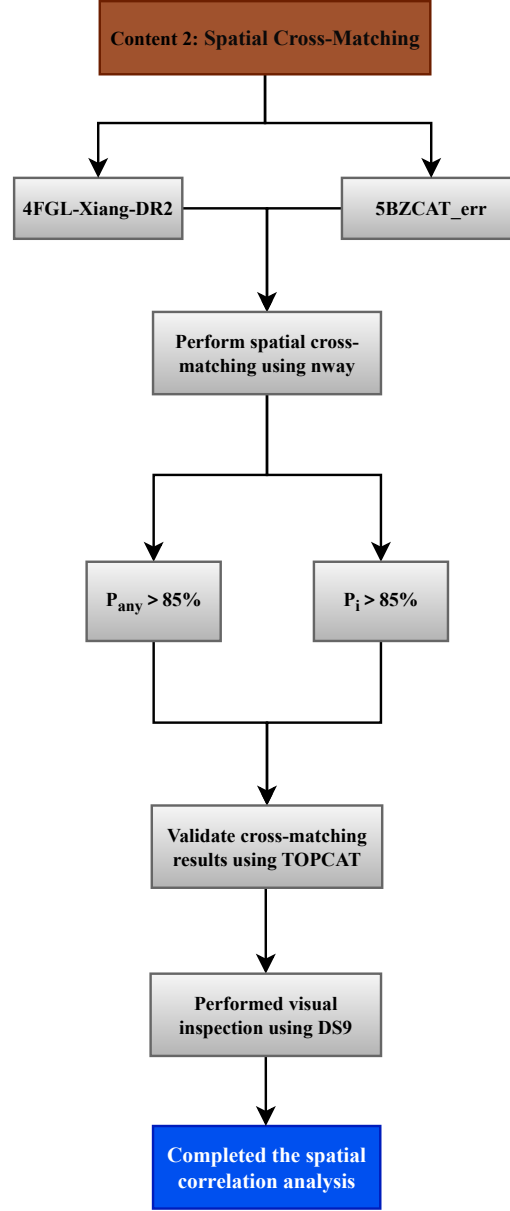
Note. Please refer to Table 6 for keyword explanations and units.

The final results satisfying the matching criteria are recorded in Table 2. The results indicate that 17 matched pairs exhibit significant spatial correlation. For the remaining matching candidates with lower probabilities, we performed a visual inspection using the plotting script **nway-explain.py** provided by **nway**, revealing that they exhibit a low degree of positional coincidence. Given the substantial amount of data requiring manual inspection in this step, and to prevent the oversight of cross-identified results due to complicated procedures, we utilized the efficient cross-matching functionality provided by **TOPCAT** (see M. B. Taylor 2005) to perform an additional verification of the cross-matching results between DR2 and 5BZCAT_err. **TOPCAT** is a widely used data analysis tool for spatial

Table 8. Positional Data and Uncertainty of 5BZCAT_err

Name	RA	DEC	Conf95_Maj	Conf95_Min	Unc_PA	Refcode	Opt_Mag
5BZB J0001-0011	0.340	-0.194	0.209	0.209	0	2013wise.rept....1C	19.6
5BZB J0001-0746	0.325	-7.774	0.105	0.101	90	2013wise.rept....1C	17.9
5BZB J0002-0024	0.738	-0.413	0.150	0.150	0	2007ApJS..171...61H	19.7
...

Note. Please refer to Table 6 for keyword explanations and units, and see Section 5 for the full contents of the table.

**Figure 14.** The analytical pipeline for spatial cross-matching between DR2 and 5BZCAT_err.

cross-matching, providing an efficient method for matching sources based on elliptical positional uncertainties. In this study, its primary advantage lies in its ability to rapidly perform batch cross-matching between two catalogs. Using this approach, we identified 17 matched pairs, which are fully consistent with the results obtained using the probabilistic thresholds applied in **nway**.

To more comprehensively verify the spatial association between the γ -ray emission of target sources in DR2 and the 17 blazar objects in 5BZCAT_err, we employed the **tmap()** function in **Fermipy** to generate TS maps. Subsequently, we conducted a visual inspection of the 17 cross-matched results using the **DS9** software (W. A. Joye & E. Mandel 2003). Here, we present the TS maps of three representative objects, as shown in Figure 15. The TS maps for the remaining 16 GeV sources are archived in the file **TSmap17.tar.xz**; see Section 5 for details. The results indicate that these objects exhibit a high degree of spatial correlation, further supporting the reliability of our probabilistic cross-matching approach.

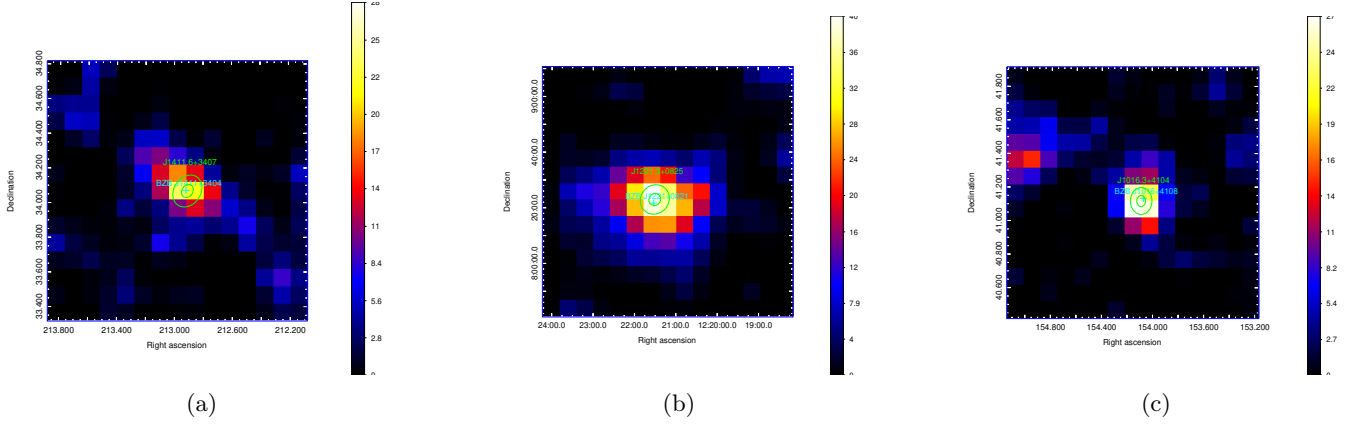


Figure 15. The TS map visualizes source cross-association, where the color scale reflects the TS value, serving as a measure of detection significance.

C. STATISTICAL ANALYSIS PIPELINE FOR MULTI-WAVELENGTH FLUX

C.1. Acquisition and Preparation of the Multi-wavelength Flux Dataset

Following the pipeline from Content 3 in Figure 14, we efficiently extract multi-wavelength flux data for blazars in 5BZCAT_err. First, we used the **astroquery.ipac.ned.get_table()** function with the parameter **table='photometry'** to retrieve flux measurements from NED. During data collection, we found that 119 sources lacked flux data in the required bands. To rule out potential issues such as network interruptions, we re-executed the **get_table()** function for these sources and confirmed that the relevant flux data were indeed unavailable. Ultimately, we successfully retrieved multi-wavelength flux data for 3,442 sources. The collected data were subsequently standardized in terms of format and units to ensure consistency for subsequent analyses. The processed dataset was uniformly stored in the file **5BZCAT_multi-band_flux.xlsx**, as referenced in Section 5. Next, based on blazar classification, the data were grouped into two categories by energy band: BZB (including both BZB and BZG) and BZQ. Sources classified as BZU were excluded from subsequent analysis due to their ambiguous classification.

C.2. Comparative Statistical Analysis of Flux Distributions

A detailed pipeline for this part is presented in Content 4 of Figure 17. To facilitate an investigation of the multi-wavelength flux distribution of 5BZCAT_err blazars, we applied a base-10 logarithmic transformation to the flux values. This approach effectively compresses the wide range of the data, significantly reduces skewness, and adheres to scientific conventions in blazar flux analysis (M. Ackermann et al. 2015). To systematically investigate the similarities and differences in the flux distributions of BZBs and BZQs across various wavebands, we employed **matplotlib.pyplot** to create frequency histograms spanning 11 wavebands (see Figure 16). Additionally, using **scipy.stats** (P. Virtanen et al. 2020), we computed eight commonly used statistical parameters to comprehensively characterize the statistical properties of the distributions from multiple dimensions.

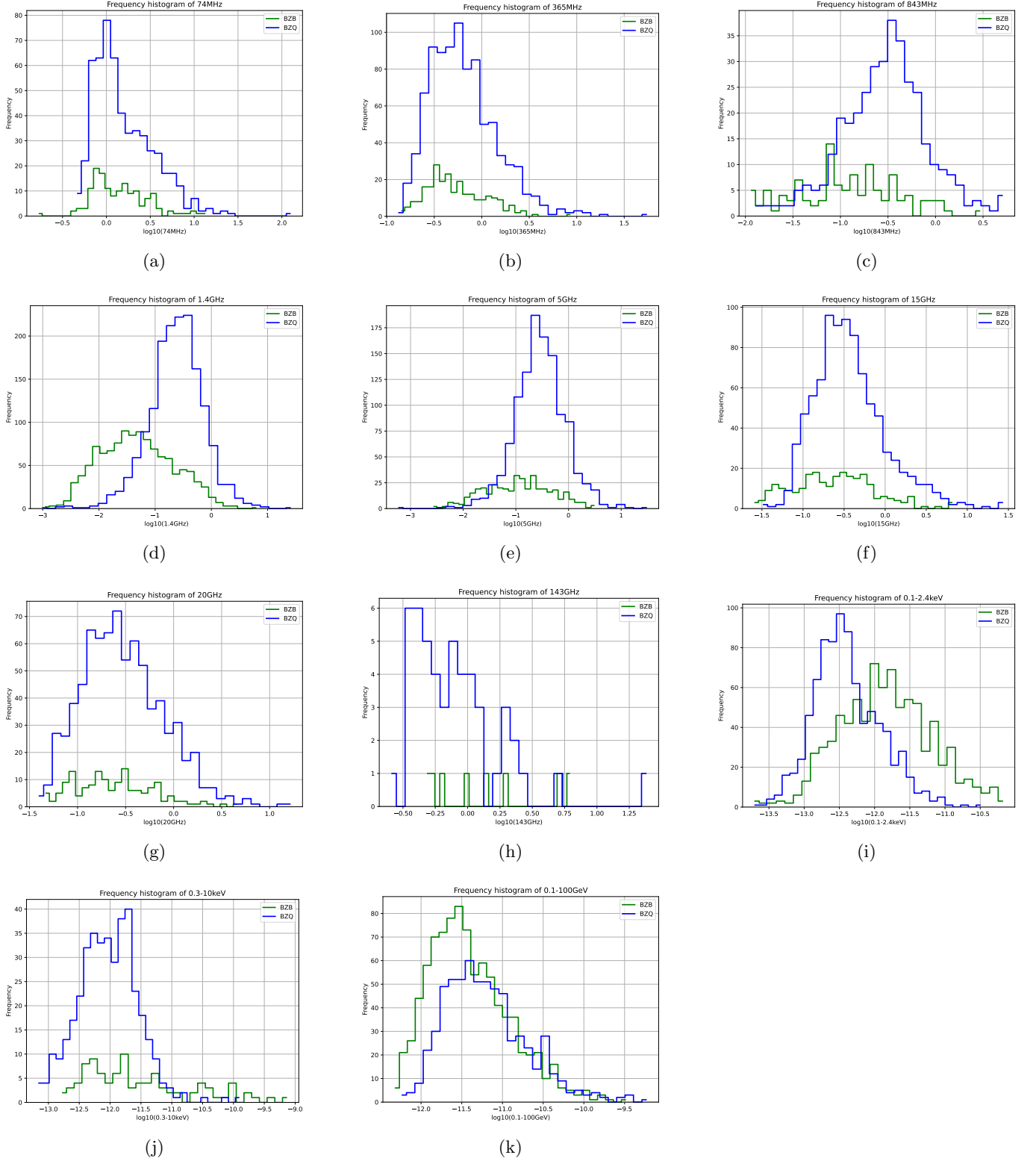


Figure 16. Frequency histograms of flux distributions for blazars in the 5BZCAT_err across 11 wavebands, showing BZBs in green and BZQs in blue, with flux values on the horizontal axis and frequency on the vertical axis.

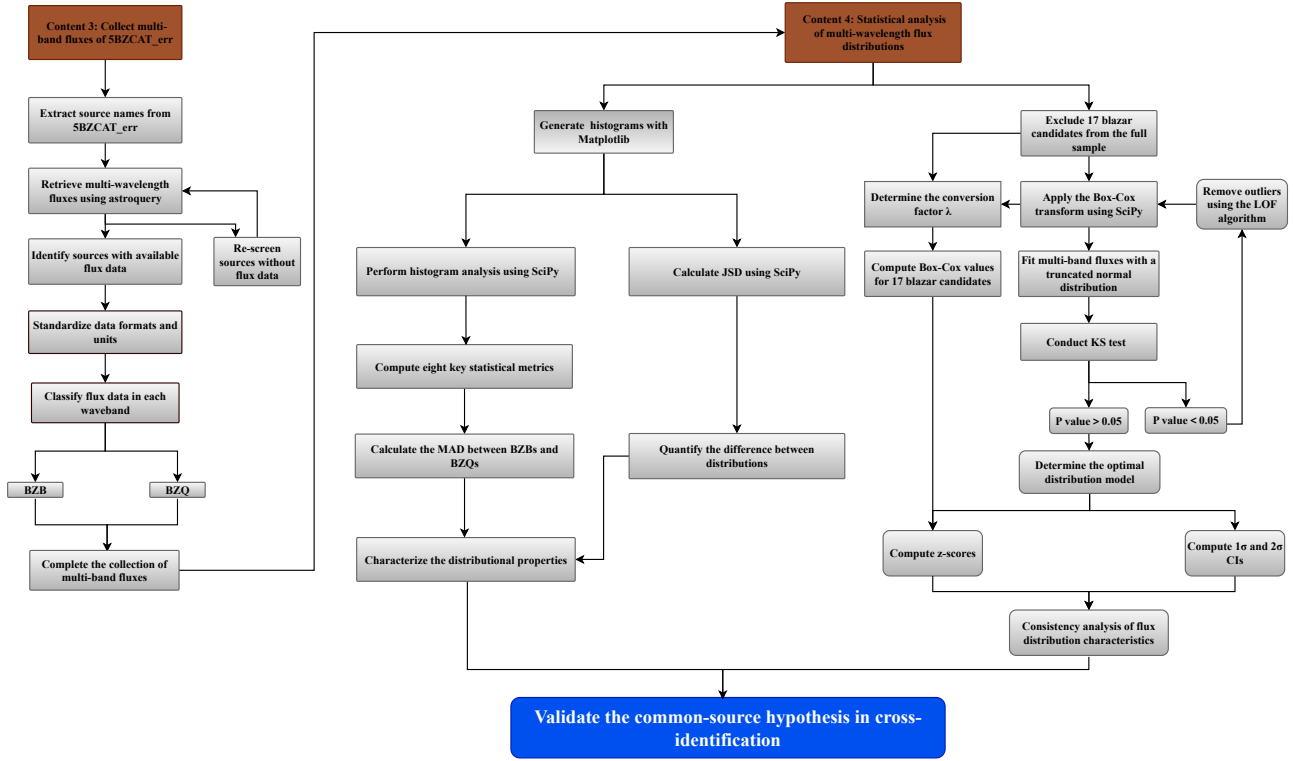


Figure 17. This figure shows the pipeline for the statistical modeling and analysis of multi-band flux distributions in blazars.

These parameters include the minimum (min), maximum (max), mean, median, mode, standard deviation (std), skewness, and kurtosis. The mean represents the average of the logarithmic flux values and reflects the overall level of the distribution. The median denotes the central value of the ordered dataset, indicating the distribution's central tendency and is less sensitive to outliers. The mode refers to the most frequently occurring value, representing the most common state within the distribution. The std reflects the dispersion of the flux data, with larger values indicating greater spread and smaller values indicating tighter concentration. Skewness measures the asymmetry of the flux distribution, where positive values indicate right skewness and negative values indicate left skewness. Kurtosis describes the sharpness of the distribution profile, with higher values indicating a more peaked distribution and lower values indicating a flatter shape. Together, these parameters collectively provide a quantitative basis for multi-wavelength flux analysis. To clearly investigate the differences in various statistical metrics between BZBs and BZQs, we plotted the relationship between each statistical metric and waveband, as shown in Figure 18, in conjunction with Table 9. To quantify the overall differences in various statistical metrics between BZBs and BZQs across different wavebands, we computed the Median Absolute Deviation (MAD) for each metric, using the following formula:

$$\text{MAD} = \frac{1}{n} \sum_{i=1}^n |S_{\text{BZQ},i} - S_{\text{BZB},i}| \quad (\text{C1})$$

where $S_{\text{BZQ},i}$ and $S_{\text{BZB},i}$ denote the values of a given statistical metric (e.g., min, max, mean, etc.) for BZQs and BZBs, respectively, in the i -th frequency band. n represents the total number of frequency bands.

The MAD value quantifies the average difference in statistical metrics between BZQs and BZBs, with smaller values indicating closer similarity and larger values implying greater disparity. Subsequently, we calculated the MAD values of eight statistical metrics for BZBs and BZQs across different wavebands, as presented in the last column of Table 9. From subfigures (a) to (e) in Figure 18, a pronounced downward trend is observed in the curves from 143 GHz to 0.1–2.4 keV. This trend is primarily attributed to the inconsistency in flux units: fluxes from 74 MHz to 143 GHz are measured in Jy, whereas those from 0.1 keV to 100 GeV are measured in $\text{erg cm}^{-2} \text{s}^{-1}$. However, this unit discrepancy

Statistical Comparison of Multiband Flux Distributions between BZQ and BZB

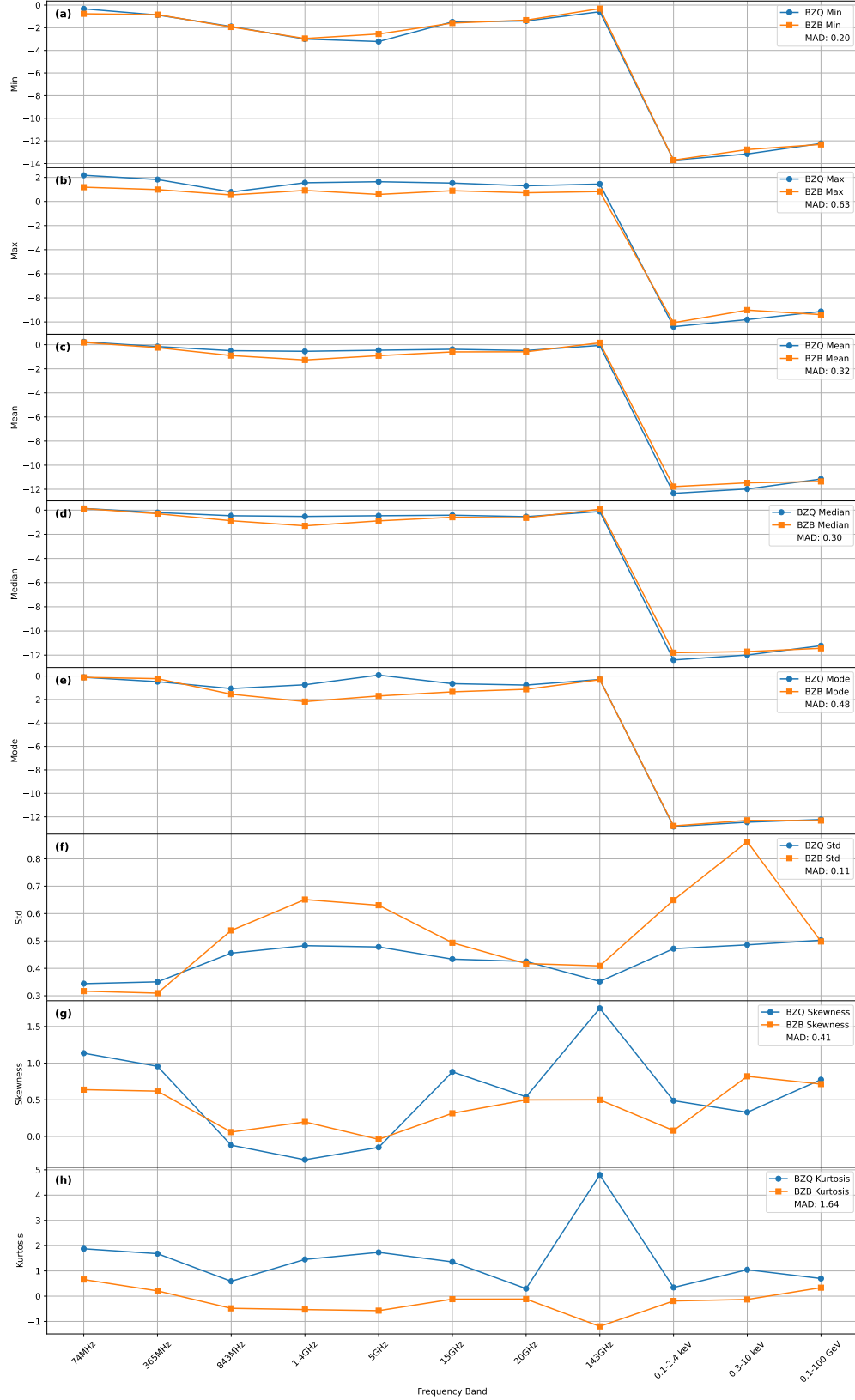


Figure 18. Comparative analysis of multiband flux statistical characteristics between BZQs and BZBs. In each subplot, the blue and orange data points represent the values of eight classical statistical metrics, calculated across 11 wavebands, for BZBs and BZQs, respectively.

Table 9. Comparative Analysis of Flux Distributions Between BZBs and BZQs

Type	Min	Max	Mean	Median	Mode	Std	Skewness	Kurtosis	JSD(BZB & BZQ)
74 MHz									
BZB	-0.76	1.19	0.18	0.13	-0.11	0.32	0.64	0.66	0.11
BZQ	-0.33	2.18	0.24	0.14	-0.11	0.34	1.14	1.88	
365 MHz									
BZB	-0.84	0.99	-0.24	-0.30	-0.22	0.31	0.62	0.21	0.12
BZQ	-0.87	1.82	-0.15	-0.20	-0.48	0.35	0.96	1.68	
843 MHz									
BZB	-1.94	0.55	-0.90	-0.88	-1.55	0.54	0.06	-0.48	0.31
BZQ	-1.89	0.79	-0.50	-0.46	-1.07	0.46	-0.12	0.59	
1.4 GHz									
BZB	-2.95	0.92	-1.26	-1.30	-2.18	0.65	0.20	-0.53	0.50
BZQ	-3.00	1.55	-0.55	-0.52	-0.74	0.48	-0.32	1.46	
5 GHz									
BZB	-2.55	0.59	-0.91	-0.89	-1.70	0.63	-0.04	-0.57	0.36
BZQ	-3.22	1.64	-0.46	-0.46	0.08	0.48	-0.15	1.73	
15 GHz									
BZB	-1.59	0.89	-0.60	-0.59	-1.35	0.49	0.32	-0.12	0.25
BZQ	-1.48	1.53	-0.38	-0.42	-0.65	0.43	0.88	1.36	
20 GHz									
BZB	-1.33	0.72	-0.59	-0.63	-1.13	0.42	0.50	-0.12	0.11
BZQ	-1.40	1.30	-0.48	-0.54	-0.77	0.43	0.54	0.30	
143 GHz									
BZB	-0.31	0.82	0.16	0.07	-0.31	0.41	0.50	-1.20	0.29
BZQ	-0.59	1.45	-0.06	-0.11	-0.29	0.35	1.75	4.80	
0.1–2.4 keV									
BZB	-13.70	-10.06	-11.78	-11.80	-12.77	0.65	0.08	-0.19	0.40
BZQ	-13.70	-10.39	-12.34	-12.40	-12.82	0.47	0.49	0.34	
0.3–10 keV									
BZB	-12.77	-9.02	-11.47	-11.71	-12.30	0.86	0.82	-0.13	0.34
BZQ	-13.15	-9.80	-11.98	-11.99	-12.46	0.49	0.33	1.05	
0.1–100 GeV									
BZB	-12.31	-9.39	-11.35	-11.43	-12.31	0.50	0.71	0.34	0.18
BZQ	-12.23	-9.13	-11.15	-11.22	-12.23	0.50	0.77	0.70	
MAD	0.20	0.63	0.32	0.30	0.48	0.11	0.41	1.64	-

Note. This table summarizes the statistical characteristics and comparative analysis results of the flux distributions for BZBs and BZQs across 11 wavebands. For each band, the min, max, mean, median, mode, std, skewness, and kurtosis of the log-transformed flux values are listed. The last row reports the Mean Absolute Difference (MAD) between BZBs and BZQs for the eight statistical metrics above, highlighting the degree of difference in individual statistical characteristics. The final column shows the JSD, which quantifies the overall statistical difference in the flux probability density distributions between BZBs and BZQs in each waveband.

has no substantial impact on the MAD-based analysis of the relevant metrics, as changes in units do not affect the relative distribution profiles of the two object classes within the same energy band. Based on the MAD values and the observed differences across statistical metrics, we draw the following conclusions:

(1) Panel (a) of Figure 18 shows that the difference in the min flux values between BZBs and BZQs is relatively small, as reflected by a MAD value of 0.2. This suggests that the lower limits of the fluxes produced by their respective radiation mechanisms are not significantly different.

(2) Panel (b) of Figure 18 reveals a substantial difference in the max flux values between BZBs and BZQs, with a corresponding MAD of 0.63. Across the 74 MHz to 143 GHz range, BZQs exhibit max flux values approximately one order of magnitude higher than those of BZBs. In the 0.3–10 keV band, the max flux value of BZBs is slightly higher than that of BZQs. However, in the 0.1–2.4 keV and 0.1–100 GeV bands, the overall difference is negligible, with the max values of BZBs and BZQs nearly overlapping.

(3) As shown in panels (c), (d), and (e) of Figure 18, the trends of the mean, median, and mode for BZQs and BZBs exhibit remarkable similarity. This similarity stems primarily from their shared mathematical properties, with all three serving as measures of central tendency in a distribution. In the radio band, particularly within the frequency range of 843 MHz to 15 GHz, the mean, median, and mode values for BZQs are consistently higher than those for BZBs. This suggests that BZQs generally exhibit stronger radio emission in these bands. In the 0.1–10 keV energy range, the mean and median values for BZBs are slightly higher than those for BZQs. Across the 0.1–100 GeV range, the values of all three metrics are similar between BZBs and BZQs, showing no significant differences.

(4) Panel (f) of Figure 18 shows the variation trends of the std for BZQs and BZBs across different frequency bands. As indicated by a MAD value of 0.11, the overall average difference in std between BZBs and BZQs is not significant. However, across the frequency range from 843 MHz to 100 GeV, the flux distributions of BZBs generally exhibit greater dispersion than those of BZQs. The std values for BZQs are mostly confined to a narrower range of 0.34–0.50, whereas those for BZBs span a broader range of 0.30–0.90. This suggests that BZB flux distributions are more widely spread, while those of BZQs are relatively more concentrated.

(5) Panel (g) of Figure 18 shows the variation of skewness for BZQs and BZBs across different wavebands. Overall, both source types exhibit positive skewness in most frequency bands, indicating that their flux distributions are right-skewed. Furthermore, the MAD of skewness between BZQs and BZBs is 0.41, suggesting notable differences in the asymmetry of their flux distributions across wavebands. This discrepancy is especially evident at 143 GHz, where the skewness of BZQ surpasses that of BZB by approximately 1.3. The skewness of the BZQ sample ranges from -0.3 to 1.8, suggesting that the asymmetry of its flux distribution varies noticeably across different energy ranges. In contrast, the skewness of the BZB sample shows a relatively smooth trend, with values primarily concentrated between 0 and 0.8, suggesting a more stable distribution structure across different wavebands.

(6) Panel (h) of Figure 18 shows that the MAD of kurtosis between BZQs and BZBs is 1.64, indicating a significant difference in the peakedness of their flux distributions. Overall, the kurtosis values for the BZQ sample are consistently higher than those for BZBs across all frequency bands, with the most significant difference observed at 143 GHz. At this frequency, the kurtosis of BZQs rises sharply to 4.8, while that of BZBs remains around -1.2. The resulting kurtosis difference of nearly 6 clearly reflects a marked distinction in their distribution characteristics.

The above MAD analysis reveals varying degrees of statistical differences in the multi-band flux distributions between BZBs and BZQs, reflecting disparities across different distributional characteristics. Among all considered metrics, kurtosis, as a statistical indicator of distributional peakedness and tail weight, exhibits the highest MAD value of 1.64. This suggests that kurtosis is likely the most effective metric for distinguishing the differences in multi-band flux distributions between BZBs and BZQs.

To more comprehensively assess the differences in the multi-band flux distributions between BZBs and BZQs, this study not only employs MAD to analyze point-to-point differences of various statistical metrics, but also introduces the Jensen–Shannon Distance (JSD) as a complementary measure. The JSD evaluates the overall difference between the two types of objects based on their probability density distributions (PDDs) and is particularly effective in capturing differences in distributional characteristics. Compared to unidimensional statistical metrics, the JSD provides a unique advantage in revealing distributional structure differences through a comprehensive assessment. When the logarithm base is 2, the JSD ranges from 0 to 1, where 0 indicates identical distributions and 1 indicates completely different ones (D. M. Endres & J. E. Schindelin 2003; R. Connor et al. 2013). In general, a value of $\text{JSD} > 0.3$ indicates a significant difference between the two distributions (D. Carton et al. 2018). Due to its boundedness, it is well-suited for the comparative analysis of probability distributions in this study.

In the analysis process, we first applied a base-10 logarithmic transformation to the flux data in each waveband. We then used the **gaussian.kde** method from the **scipy.stats** module to perform kernel density estimation (KDE), which constructs a normalized probability density function that approximates the underlying distribution of the input data via Gaussian kernel smoothing (P. Virtanen et al. 2020). Next, we used the **scipy.spatial.distance.jensenshannon**

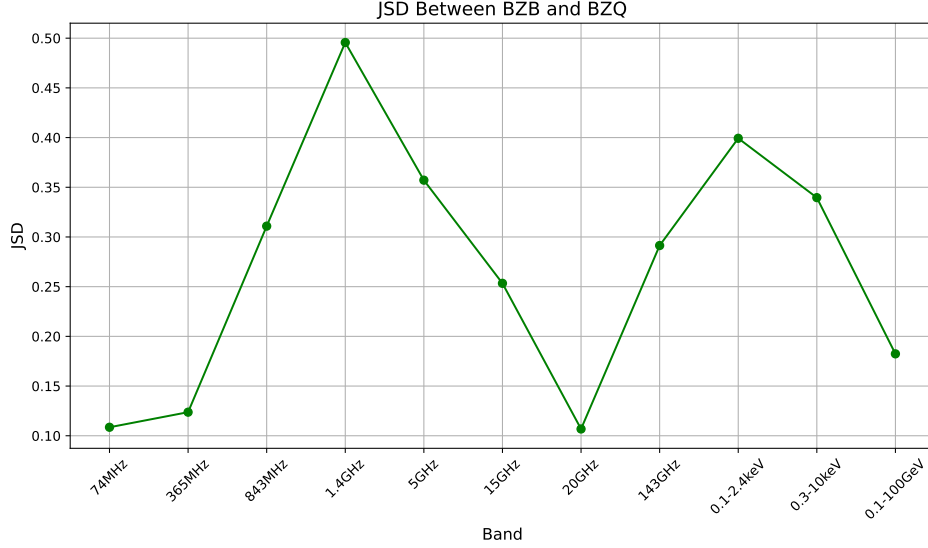


Figure 19. This figure shows the trend of JSD variation of the flux distributions between BZBs and BZQs across 11 wavebands.

function¹² to calculate the JSD values between the flux PDDs of BZBs and BZQs across 11 wavebands. The corresponding JSD results are summarized in the last column of Table 9. The JSD quantifies the divergence between two probability distributions and is derived from the Jensen–Shannon divergence, $JSD'(p, q)$, which is defined as follows:

$$JSD'(p, q) = \frac{1}{2}D(p \parallel m) + \frac{1}{2}D(q \parallel m) \quad (C2)$$

Let p and q be two probability distributions, and let $m = \frac{1}{2}(p + q)$ denote their symmetric mixture distribution. The function $D(\cdot \parallel \cdot)$ represents the Kullback–Leibler(KL) divergence. The JSD is then defined as the square root of the $JSD'(p, q)$:

$$JSD(p, q) = \sqrt{JSD'(p, q)} \quad (C3)$$

The $JSD'(p, q)$ is a symmetrized measure of distributional difference based on the KL divergence, as introduced by J. Lin (2002). The KL divergence quantifies the information loss incurred when one probability distribution is used to approximate another, and is defined as follows (J. R. Hershey & P. A. Olsen 2007):

$$D(p \parallel m) = \int p(x) \log \frac{p(x)}{m(x)} dx, \quad D(q \parallel m) = \int q(x) \log \frac{q(x)}{m(x)} dx \quad (C4)$$

To intuitively analyze the variation trend of JSD across different wavebands, we plotted the JSD data from Table 9 in Figure 19. Figure 19 illustrates notable differences in the probability distributions of BZBs and BZQs across various wavebands, especially at 1.4 GHz and 0.1–2.4 keV, where the JSD values exceed 0.3. In contrast, the JSD values at 74 MHz and 20 GHz are below 0.15, indicating relatively small differences in flux distributions between the two source types. This may suggest that BZBs and BZQs share similar radiative characteristics in these low-energy bands. Overall, the trend of JSD variation shown in Figure 19 highlights the varying degrees of distributional divergence between BZBs and BZQs across different wavebands.

The above analysis shows that the MAD values of the eight classical statistical measures and the JSD values across different wavebands are all greater than zero, indicating systematic differences in the flux distributions between BZBs and BZQs. A univariate analysis using MAD as the difference metric reveals that the two source types differ significantly in max, mode, skewness, and kurtosis, with corresponding MAD values exceeding 0.4. Among these, kurtosis shows the largest discrepancy, with a MAD value of 1.64. Using JSD as a metric, we identified substantial differences in the probability distributions of the two source types at 1.4 GHz and 0.1–2.4 keV, where the JSD values exceed 0.3 and

¹² <https://docs.scipy.org/doc/scipy/reference/generated/scipy.spatial.distance.jensenshannon.html>

are markedly higher than those in other wavebands. These distributional differences can also be clearly observed from the probability density function (PDF) curves generated by KDE, as shown in Figure 20. The distribution differences

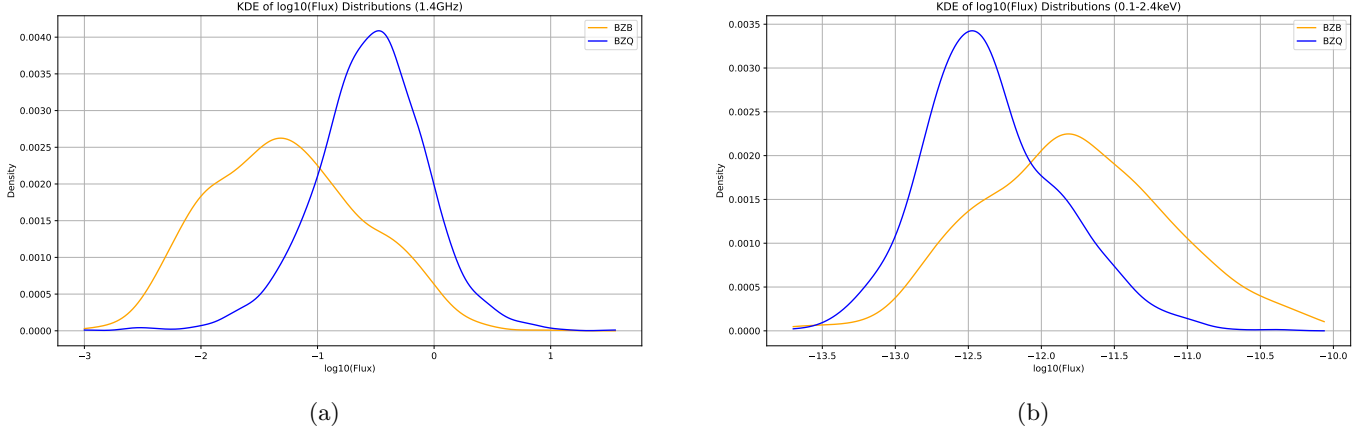


Figure 20. Kernel density estimations of the $\log_{10}(\text{Flux})$ distributions at 1.4 GHz and 0.1-2.4 keV for BZBs and BZQs.

in other wavebands, whether analyzed using MAD or JSD, are relatively small but still objectively present.

In conclusion, we find that the two types of blazars exhibit systematic differences in their radiation behaviors across multiple wavebands. These differences are reflected not only in the central tendencies of the distributions but also in their skewness and kurtosis.

C.3. Statistical Modeling Scheme

A detailed description of the pipeline is presented in Content 4 of Figure 17, and the specific modeling steps are outlined as follows:

First, the 17 new GeV blazar candidates are excluded from the overall sample and designated as test objects for subsequent validation. Then, the flux data in each waveband are transformed using the Box-Cox transformation, implemented via the `scipy.stats.boxcox()` function. This transformation, originally proposed by G. E. Box & D. R. Cox (1964), aims to convert non-normally distributed data into an approximately normal form, thereby better satisfying the normality assumption required for subsequent statistical modeling. Its mathematical form is given as follows:

$$y = \begin{cases} \frac{x^\lambda - 1}{\lambda}, & \lambda \neq 0 \\ \ln(x), & \lambda = 0 \end{cases} \quad (\text{C5})$$

Here, λ denotes the transformation parameter, with the optimal value determined through max likelihood estimation (MLE).

For each flux dataset, the `boxcox()` function automatically determines a unique transformation parameter λ via MLE, yielding a strictly monotonic and invertible mapping between the original and transformed data. For each of the 11 observational bands, the Box-Cox transformation was applied separately to the flux distributions of BZBs and BZQs, with the optimal λ value independently estimated for each waveband. Next, we employed a TND model, implemented via `scipy.stats.truncnorm`, to fit the Box-Cox transformed flux data. The TND is constructed by constraining and renormalizing the standard normal distribution (SND) within a finite interval $[a, b]$, making it well-suited for modeling flux data that are naturally bounded due to physical constraints or observational limitations.

Let the observation interval be $[a, b]$, with its PDF given by:

$$f(x | \mu, \sigma, a, b) = \frac{1}{\sigma} \frac{\varphi\left(\frac{x-\mu}{\sigma}\right)}{\Phi\left(\frac{b-\mu}{\sigma}\right) - \Phi\left(\frac{a-\mu}{\sigma}\right)}, \quad a \leq x \leq b, \quad (\text{C6})$$

where μ and σ represent the mean and std of the original SND. The parameters a and b denote the lower and upper truncation bounds. The PDF of the SND is given by $\varphi(z) = \frac{1}{\sqrt{2\pi}} e^{-z^2/2}$, and its cumulative distribution function

(CDF) is expressed as $\Phi(z) = \int_{-\infty}^z \varphi(t) dt$. The term $\Phi\left(\frac{b-\mu}{\sigma}\right) - \Phi\left(\frac{a-\mu}{\sigma}\right)$ serves as a normalization factor, ensuring that the $f(x | \mu, \sigma, a, b)$ integrates to one over the interval $[a, b]$. The parameters μ and σ are estimated via MLE. The `scipy.stats.truncnorm.fit()` function provides a convenient tool for fitting the flux data with a TND in our analysis.

To evaluate the goodness of fit of the TND to the transformed data, we employ the Kolmogorov–Smirnov (KS) test (F. J. Massey Jr 1951). The KS test is a non-parametric method that assesses whether a sample follows a specified distribution by comparing the max absolute difference between the empirical distribution function of the transformed data and the CDF of the TND. We utilized the `scipy.stats.kstest()` function to perform the KS test, using the TND obtained from `truncnorm()` in the previous step as the reference distribution. The KS statistic and its corresponding p-value are used to evaluate the goodness of fit. If the p-value exceeds 0.05, the null hypothesis that the sample follows a TND cannot be rejected, indicating that the model provides a reasonable fit. This test is independently applied to the flux data of BZBs and BZQs in each waveband. During the preliminary fitting stage, the BZQ subsample at 74 MHz failed to pass the KS test for the TND, yielding a p -value below 0.05. This result may be attributed to the presence of outliers—data points that deviate substantially from the majority of observations—possibly arising from measurement errors or rare physical phenomena. These outliers may distort the data distribution and undermine the validity of the assumed PDF model.

To systematically identify and remove potential outliers, we applied the Local Outlier Factor (LOF) algorithm (M. M. Breunig et al. 2000) to the raw 74 MHz flux data prior to the Box–Cox transformation. The LOF method evaluates the degree of abnormality of a data point by comparing its local reachability density with that of its neighbors, thereby detecting local outliers in the data distribution. This algorithm can be conveniently implemented using the `sklearn.neighbors.LocalOutlierFactor` class¹³.

To determine the optimal hyperparameters for LOF, we conducted an exhaustive grid search over two key parameters: the neighborhood size (`n_neighbors`) and the contamination proportion (`contamination`). The neighborhood size was varied from 5 to 50 in increments of one, while the contamination proportion ranged from 0.01 to 0.20 in steps of 0.01. A total of $46 \times 20 = 920$ parameter combinations were evaluated. For each configuration, outliers were identified in the complete 74 MHz flux dataset. The resulting cleaned dataset was then fitted using the TND, and the goodness of fit was assessed via the KS test. Only configurations yielding a p-value greater than 0.05 were retained. Among all parameter combinations that passed the KS test, we selected the configuration with the lowest contamination level (`n_neighbors = 6`, `contamination = 0.07`). This selection effectively balances outlier removal with maximal preservation of the original dataset for subsequent analysis. The identified outliers are presented in Table 10. Subsequently, the Box–Cox transformation and TND fitting were re-applied to the 74 MHz BZQ flux data after outlier removal, followed by a KS test. The results confirmed consistency with the assumed distribution model, with $p > 0.05$.

In subsequent simulations, we observed that, except for the BZQ flux distribution at 74 MHz, the fitting results for all other wavebands passed the KS test without the need for outlier removal. The fitting results are summarized in Table 11, which indicates low KS statistics across all wavebands and corresponding p-values consistently greater than 0.05. These results demonstrate the broad applicability of the TND, offering a robust fit to the Box–Cox transformed flux distributions in all wavebands.

ACKNOWLEDGEMENTS

We sincerely appreciate the data and analysis software provided by the Fermi Science Support Center and also thank the support for this work from the Doctoral Initiation Fund of West China Normal University (22kE040), the Open Fund of Key Laboratory of Astroparticle Physics of Yunnan Province (2022Zibian3), and the National Natural Science Foundation of China (NSFC, Grant No. 12303048). XP is supported by Doctoral Initiation Grant 493150 from China West Normal University.

Facility: Fermi (LAT)

¹³ <https://scikit-learn.org/stable/modules/generated/sklearn.neighbors.LocalOutlierFactor.html>

Table 10. Outlier Data Identified by LOF Analysis at 74 MHz

Name	74 MHz	Uncertainty	Units	Refcode
5BZQ J0005+3820	0.79	0.12	Jy	2007AJ....134.1245C
5BZQ J0010+1724	0.79	0.12	Jy	2007AJ....134.1245C
5BZQ J0032-2649	1.01	0.13	Jy	2007AJ....134.1245C
5BZQ J0111-1317	0.95	0.13	Jy	2007AJ....134.1245C
5BZQ J0126+2559	3.36	0.35	Jy	2007AJ....134.1245C
5BZQ J0153-3310	1.03	0.18	Jy	2007AJ....134.1245C
5BZQ J0218-0923	0.72	0.12	Jy	2007AJ....134.1245C
5BZQ J0231+1322	4.11	0.45	Jy	2007AJ....134.1245C
5BZQ J0252-2219	1.18	0.13	Jy	2007AJ....134.1245C
5BZQ J0416-1851	0.69	0.11	Jy	2007AJ....134.1245C
5BZQ J0457+0645	0.95	0.14	Jy	2007AJ....134.1245C
5BZQ J0509+1011	0.95	0.16	Jy	2007AJ....134.1245C
5BZQ J0533+4822	0.97	0.13	Jy	2007AJ....134.1245C
5BZQ J0559+5804	0.71	0.10	Jy	2007AJ....134.1245C
5BZQ J0710+4220	0.97	0.13	Jy	2007AJ....134.1245C
5BZQ J0719+3307	0.71	0.09	Jy	2007AJ....134.1245C
5BZQ J0945+4636	0.71	0.10	Jy	2007AJ....134.1245C
5BZQ J0946+1017	1.18	0.16	Jy	2007AJ....134.1245C
5BZQ J1031+6020	0.69	0.09	Jy	2007AJ....134.1245C
5BZQ J1058+1951	14.83	1.51	Jy	2007AJ....134.1245C
5BZQ J1155+0214	1.03	0.13	Jy	2007AJ....134.1245C
5BZQ J1229+0203	149.96	15.00	Jy	2007AJ....134.1245C
5BZQ J1256-0547	30.63	3.06	Jy	2007AJ....134.1245C
5BZQ J1322+2148	1.01	0.15	Jy	2007AJ....134.1245C
5BZQ J1322-0937	1.16	0.15	Jy	2007AJ....134.1245C
5BZQ J1357-1527	0.79	0.14	Jy	2007AJ....134.1245C
5BZQ J1415-0955	1.03	0.16	Jy	2007AJ....134.1245C
5BZQ J1423-2218	1.16	0.17	Jy	2007AJ....134.1245C
5BZQ J1432-1801	1.18	0.15	Jy	2007AJ....134.1245C
5BZQ J1500+4751	0.97	0.13	Jy	2007AJ....134.1245C
5BZQ J1617+0246	1.01	0.16	Jy	2007AJ....134.1245C
5BZQ J1635+3808	3.36	0.34	Jy	2007AJ....134.1245C
5BZQ J2038+5119	23.72	2.44	Jy	2007AJ....134.1245C
5BZQ J2110-0126	0.69	0.11	Jy	2007AJ....134.1245C
5BZQ J2136+0041	2.22	0.23	Jy	2007AJ....134.1245C
5BZQ J2150-2812	1.01	0.12	Jy	2007AJ....134.1245C
5BZQ J2206-1835	14.48	1.50	Jy	2007AJ....134.1245C
5BZQ J2225-0457	25.64	2.57	Jy	2007AJ....134.1245C
5BZQ J2346+0930	2.23	0.24	Jy	2007AJ....134.1245C

Software: **Fermipy** (M. Wood 2017), **DS9** (W. A. Joye & E. Mandel 2003), **SciPy** (P. Virtanen et al. 2020), **Matplotlib** (J. D. Hunter 2007), **nway** (M. Salvato et al. 2018), **astroquery** (A. Ginsburg et al. 2019), **sklearn** (F. Pedregosa et al. 2011), **TOPCAT** (M. B. Taylor 2005).

REFERENCES

- Abdo, A., Ackermann, M., Ajello, M., et al. 2010a, ApJ, 715, 429
- Abdo, A., Ackermann, M., Agudo, I., et al. 2010b, ApJ, 716, 30

Table 11. Distribution Fitting Results Across 11 Wavebands

Waveband	Type	λ	Mean	Std	KS	p	TruncNorm
74 MHz	BZB	-0.257	0.343	0.635	0.069	0.459	✓
	BZQ	-0.462	0.389	0.542	0.059	0.053	✓
365 MHz	BZB	-0.334	-0.708	0.829	0.045	0.677	✓
	BZQ	-0.376	-0.507	0.863	0.026	0.568	✓
843 MHz	BZB	-0.020	-2.122	1.291	0.061	0.754	✓
	BZQ	0.031	-1.106	1.011	0.042	0.522	✓
1.4 GHz	BZB	-0.058	-3.235	1.765	0.033	0.163	✓
	BZQ	0.064	-1.175	1.022	0.026	0.202	✓
5 GHz	BZB	0.015	-2.036	1.408	0.041	0.476	✓
	BZQ	0.028	-1.026	1.070	0.033	0.168	✓
15 GHz	BZB	-0.105	-1.552	1.300	0.060	0.315	✓
	BZQ	-0.264	-1.140	1.191	0.019	0.919	✓
20 GHz	BZB	-0.213	-1.691	1.249	0.072	0.383	✓
	BZQ	-0.199	-1.364	1.192	0.029	0.506	✓
143 GHz	BZB	-0.397	0.188	0.780	0.252	0.605	✓
	BZQ	-0.593	-0.323	0.739	0.082	0.867	✓
0.1–2.4 keV	BZB	-0.019	-35.573	2.510	0.023	0.774	✓
	BZQ	-0.146	-428.554	66.794	0.037	0.187	✓
0.3–10 keV	BZB	-0.208	-1264.802	448.497	0.092	0.365	✓
	BZQ	-0.076	-94.040	9.017	0.041	0.513	✓
0.1–100 GeV	BZB	-0.240	-2275.603	576.960	0.026	0.546	✓
	BZQ	-0.236	-1874.681	471.034	0.025	0.806	✓

Note. See Table 6 for keyword explanations and units.

- Abdo, A. A., Ackermann, M., Ajello, M., et al. 2009, *ApJS*, 183, 46
- Abdo, A. A., Ackermann, M., Ajello, M., et al. 2010, *ApJS*, 188, 405
- Abdollahi, S., Acero, F., Ackermann, M., et al. 2020, *ApJS*, 247, 33
- Abdollahi, S., Acero, F., Baldini, L., et al. 2022, *ApJS*, 260, 53
- Acero, F., Ackermann, M., Ajello, M., et al. 2015, *ApJS*, 218, 23
- Ackermann, M., Ajello, M., Allafort, A., et al. 2011, *ApJ*, 743, 171
- Ackermann, M., Ajello, M., Atwood, W., et al. 2015, *ApJ*, 810, 14
- Aharonian, F. 2000, *New Astron.*, 5, 377
- Aharonian, F., Akhperjanian, A., Bazer-Bachi, A., et al. 2006, *Nature*, 440, 1018
- Ajello, M., Gasparrini, D., Sánchez-Conde, M., et al. 2015, *ApJL*, 800, L27
- Ajello, M., Baldini, L., Ballet, J., et al. 2022a, *ApJS*, 263, 24
- Ajello, M., Baldini, L., Ballet, J., et al. 2022b, *The Astrophysical Journal Supplement Series*, 263, 24
- Angel, J. R. P., & Stockman, H. 1980, *ARA&A*, 18, 321
- Atwood, W., Abdo, A. A., Ackermann, M., et al. 2009, *ApJ*, 697, 1071
- Ballet, J., Bruel, P., Burnett, T., Lott, B., et al. 2023, *arXiv preprint arXiv:2307.12546*
- Baring, M. G., Böttcher, M., & Summerlin, E. J. 2017, *MNRAS*, 464, 4875
- Blandford, R., & Eichler, D. 1987, *Phys. Rep.*, 154, 1
- Blandford, R., & Königl, A. 1979, *ApJ*, 232, 34
- Blandford, R., Rees, M., & Wolfe, A. 1978, *AM Wolfe*, Ed, 328
- Blandford, R. D., & Payne, D. 1982, *MNRAS*, 199, 883
- Blandford, R. D., & Znajek, R. L. 1977, *MNRAS*, 179, 433
- Böttcher, M., Reimer, A., Sweeney, K., & Prakash, A. 2013, *ApJ*, 768, 54
- Box, G. E., & Cox, D. R. 1964, *J. R. Stat. Soc. Series B*, 26, 211
- Breunig, M. M., Kriegel, H.-P., Ng, R. T., & Sander, J. 2000, in *Proceedings of the 2000 ACM SIGMOD international conference on Management of data*, 93–104
- Capdessus, R., King, M., Del Sorbo, D., et al. 2018, *Scientific reports*, 8, 9155
- Carton, D., Brinchmann, J., Contini, T., et al. 2018, *MNRAS*, 478, 4293
- Chen, Y.-Y., Zhang, X., Xiong, D.-R., Wang, S.-J., & Yu, X.-L. 2016, *RAA*, 16, 013
- Cheng, Z. 2008, *Highlights in Science, Engineering and Technology*, Vol. 94 (Darcy & Roy Press), 442
- Connor, R., Cardillo, F. A., Moss, R., & Rabitti, F. 2013, in *International Conference on Similarity Search and Applications*, Springer, 163–168

- DasGupta, A. 2008, *Asymptotic theory of statistics and probability*, Vol. 180 (Springer)
- Dermer, C. D., & Giebels, B. 2016, *C. R. Phys.*, 17, 594
- Endres, D. M., & Schindelin, J. E. 2003, *IEEE Trans. Inf. Theory*, 49, 1858
- Fan, J., Yang, J., Liu, Y., et al. 2016, *ApJS*, 226, 20
- Fan, J., Yang, J., Xiao, H., et al. 2017, *ApJL*, 835, L38
- Foschini, L., Dalla Barba, B., Tornikoski, M., et al. 2024, *Universe*, 10, 156
- Fossati, G. a., Maraschi, L., Celotti, A., Comastri, A., & Ghisellini, G. 1998, *MNRAS*, 299, 433
- Freedman, W. L., & Madore, B. F. 2010, *Annual Review of Astronomy and Astrophysics*, 48, 673
- Ghisellini, G., Celotti, A., Fossati, G., Maraschi, L., & Comastri, A. 1998, *MNRAS*, 301, 451
- Ghisellini, G., Tavecchio, F., Foschini, L., & Ghirlanda, G. 2011, *MNRAS*, 414, 2674
- Giannios, D., Uzdensky, D. A., & Begelman, M. C. 2009, *MNRAS Lett.*, 395, L29
- Ginsburg, A., Sipőcz, B. M., Brasseur, C., et al. 2019, *AJ*, 157, 98
- Hershey, J. R., & Olsen, P. A. 2007, 4, IV
- Hunter, J. D. 2007, *Computing in science & engineering*, 9, 90
- Hyndman, R. J., & Fan, Y. 1996, *The American Statistician*, 50, 361
- Ialongo, C. 2019, *Biochem. Med.*, 29, 5
- Joye, W. A., & Mandel, E. 2003, in *Astronomical data analysis software and systems XII*, Vol. 295, 489
- Lande, J., Ackermann, M., Allafort, A., et al. 2012, *ApJ*, 756, 5
- Lin, J. 2002, *IEEE Trans. Inf. Theory*, 37, 145
- Liodakis, I., Marscher, A. P., Agudo, I., et al. 2022, *Nature*, 611, 677
- Lister, M., Aller, M., Aller, H., et al. 2011, *ApJ*, 742, 27
- Madejski, G., & Sikora, M. 2016, *ARA&A*, 54, 725
- Mannheim, K. 1993, *A&A*, 269, 67
- Mannheim, K., & Biermann, P. 1992, *A&A*, 253, L21
- Maraschi, L., Ghisellini, G., & Celotti, A. 1992, *ApJ*, 397, L5
- Massaro, E., Giommi, P., Leto, C., et al. 2009, *A&A*, 495, 691
- Massaro, E., Maselli, A., Leto, C., et al. 2015, *Astrophys. Space Sci.*, 357, 1
- Massaro, F., D’Abrusco, R., Tosti, G., et al. 2012, *ApJ*, 750, 138
- Massey Jr, F. J. 1951, *JASA*, 46, 68
- Mei, D.-C., Xie, G.-Z., Qin, Y.-P., Bai, J.-M., & Cheng, L.-E. 1999, *PASJ*, 51, 579
- Mücke, A., & Protheroe, R. 2001, *Astropart. Phys.*, 15, 121
- Mücke, A., Protheroe, R., Engel, R., Rachen, J., & Stanev, T. 2003, *Astropart. Phys.*, 18, 593
- NASA/IPAC Extragalactic Database. 2019, NASA/IPAC Extragalactic Database, IPAC, doi: [10.26132/NED1](https://doi.org/10.26132/NED1)
- Nolan, P. L., Abdo, A., Ackermann, M., et al. 2012, *ApJS*, 199, 31
- Oke, J. B., & Sandage, A. 1968, *Astrophysical Journal*, vol. 154, p. 21, 154, 21
- Pedregosa, F., Varoquaux, G., Gramfort, A., et al. 2011, *J. Mach. Learn. Res.*, 12, 2825
- Rice, J. A., & Rice, J. A. 2007, *Mathematical statistics and data analysis*, Vol. 371 (Thomson/Brooks/Cole Belmont, CA)
- Rousseeuw, P. J., & Hubert, M. 2011, *WIREs Data Min. Knowl. Discov.*, 1, 73
- Roy, S., & Suyama, T. 2024, *Results Phys.*, 61, 107757
- Salvato, M., Buchner, J., Budavári, T., et al. 2018, *MNRAS*, 473, 4937
- Sbarrato, T., Ghisellini, G., Maraschi, L., & Colpi, M. 2012, *MNRAS*, 421, 1764
- Shaikh, S. A., & Kitagawa, H. 2014, *World Wide Web*, 17, 511
- Sikora, M., Begelman, M. C., & Rees, M. J. 1994, *ApJ*, 421, 153
- Sironi, L., & Spitkovsky, A. 2014, *ApJL*, 783, L21
- Stawarz, L., & Petrosian, V. 2008, *ApJ*, 681, 1725
- Tavecchio, F. 2021, *Galaxies*, 9, 37
- Tavecchio, F., Maraschi, L., Pian, E., et al. 2001, *ApJ*, 554, 725
- Taylor, M. B. 2005, in *Astronomical data analysis software and systems XIV*, Vol. 347, 29
- Urry, C. M., & Padovani, P. 1995, *PASP*, 107, 803
- Virtanen, P., Gommers, R., Oliphant, T. E., et al. 2020, *Nature methods*, 17, 261
- Volonteri, M., Haardt, F., Ghisellini, G., & Ceca, R. D. 2011, *MNRAS*, 416, 216
- Wills, B. J., & Brotherton, M. 1995, *ApJ*, 448, L81
- Wills, B. J., Wills, D., Breger, M., Antonucci, R., & Barvainis, R. 1992, *ApJ*, 398, 454
- Wood, M. 2017, *PoS*, 824
- Xiang, Y., Feng, P., & Lan, X. 2024, *RAA*, 24, 105004
- Xiao, H., Ouyang, Z., Zhang, L., et al. 2022, *ApJ*, 925, 40
- Xie, S., Ouyang, Z., Wu, J., et al. 2024, *ApJ*, 976, 78
- Yang, W., Wang, H., Liu, Y., et al. 2022, *ApJ*, 925, 120
- Zhou, J., & Su, Y. 2006, *Proceedings of the International Astronomical Union*, 2, 477–478